Electronic Structure of High-Spin Iron(III)−Alkylperoxo Complexes and Its Relation to Low-Spin Analogues: Reaction Coordinate of O−O Bond Homolysis

Nicolai Lehnert,[†] Raymond Y. N. Ho,[‡] Lawrence Que, Jr.,[‡] and Edward I. Solomon*[,†]

Contribution from the Department of Chemistry, Stanford University, Stanford, California 94305-5080, and Department of Chemistry and Center for Metals in Biocatalysis, University of Minnesota, Minneapolis, Minnesota 55455

Received June 13, 2001

Abstract: The spectroscopic properties of the high-spin Fe(III)−alkylperoxo model complex $[Fe(6\text{-}Me_3TPA)(OH_x)(OO^tBu)]^{x+}$ (**1**; TPA = tris(2-pyridylmethyl)amine, ^tBu = *tert*-butyl, $x = 1$ or 2) are defined and related to density functional calculations of corresponding models in order to determine the electronic structure and reactivity of this system. The Raman spectra of **1** show four peaks at 876, 842, 637, and 469 cm^{-1} that are assigned with the help of normal coordinate analysis, and corresponding force constants have been determined to be 3.55 mdyn/Å for the O−O and 2.87 mdyn/Å for the Fe−O bond. Complex **1** has a broad absorption feature around 560 nm that is assigned to a charge-transfer (CT) transition from the alkylperoxo π_v^* to a t_{2g} d orbital of Fe(III) with the help of resonance Raman profiles and MCD spectroscopy. An additional contribution to the Fe−O bond arises from a σ interaction between π_h^* and an e_g d orbital of iron. The electronic structure of **1** is compared to the related low-spin model complex $[Fe(TPA)(OH_x)(OO^tBu)]^{x+}$ and the reaction coordinate for O−O homolysis is explored for both the low-spin and the high-spin Fe(III)−alkylperoxo systems. Importantly, there is a barrier for homolytic cleavage of the O−O bond on the high-spin potential energy surface that is not present for the low-spin complex, which is therefore nicely set up for O−O homolysis. This is reflected by the electronic structure of the low-spin complex having a strong Fe−O and a weak O−O bond due to a strong Fe−O σ interaction. In addition, the reaction coordinate of the Fe−O homolysis has been investigated, which is a possible decay pathway for the high-spin system, but which is thermodynamically unfavorable for the low-spin complex.

Introduction

Mononuclear non-heme iron enzymes catalyze a variety of different oxidation and hydroxylation reactions of substrates. These systems include intra- and extradiol dioxygenases (oxidative cleavage of dihydroxylated aromatic rings), pterin-dependent hydroxylases (monohydroxylation of aromatic rings), α-ketoglutarate dependent enzymes (monohydroxylation and ring closure), lipoxygenase (hydroperoxidation of fatty acids), and Rieske-type dioxygenases (dihydroxylation of aromatic rings).[1,2] For a number of these enzymes, high-spin Fe(III)−alkyl- and hydroperoxo complexes have been proposed to occur along the reaction coordinate. However, no such intermediate has yet been isolated.[3] Prominent species that have been studied experimentally are purple lipoxygenase, which is a high-spin Fe(III)−alkylperoxo (enzyme−product) complex[4−7] and activated bleomycin (ABLM), which is a low-spin Fe(III)−OOH complex of the anticancer drug bleomycin that is capable of cleaving DNA.[8−14]

A number of related inorganic model complexes have been synthesized, and their reactivity toward different substrates has been investigated.[3] The low-spin Fe(III)−alkylperoxo complex $[Fe(TPA)(OH_x)(OO^tBu)]^{x+}$ (TPA = tris(2-pyridylmethyl)amine, $x = 1$ or 2[15])[16−18] has been intensively studied and experimentally shown to undergo homolytic cleavage of

[†] Stanford University.

[‡] University of Minnesota.

(1) Holm, R. H.; Kennepohl, P.; Solomon, E. I. *Chem. Rev.* **1996**, *96*, 2239.

(2) Que, L., Jr.; Ho, R. Y. N. *Chem. Rev.* **1996**, *96*, 2607.

(3) Solomon, E. I.; Brunold, T. C.; Davis, M. I.; Kemsley, J. N.; Lee, S.-K.; Lehnert, N.; Neese, F.; Skulan, A. J.; Yang, Y.-S.; Zhou, J. *Chem. Rev.* **2000**, *100*, 235.

(4) De Groot, J. J. M. C.; Garssen, G. J.; Veldink, G. A.; Vliegenthart, J. F. G.; Boldingh, J. *FEBS Lett.* **1975**, *56*, 50.

(5) Spaapen, L. J. M.; Veldink, G. A.; Liefkens, T. J.; Vliegenthart, J. F. G.; Kay, C. M. *Biochim. Biophys. Acta* **1979**, *574*, 301.

(6) Slappendel, S.; Veldink, G. A.; Vliegenthart, J. F. G.; Aasa, R.; Malmström, B. G. *Biochim. Biophys. Acta* **1983**, *747*, 32.

(7) Nelson, M. J.; Chase, D. B.; Seitz, S. P. *Biochemistry* **1995**, *34*, 6159.

(8) Burger, R. M.; Peisach, J.; Horwitz, S. B. *J. Biol. Chem.* **1981**, *256*, 11636.

(9) Burger, R. M.; Kent, T. A.; Horwitz, S. B.; Münck, E.; Peisach, J. *J. Biol. Chem.* **1983**, *258*, 1559.

(10) Sam, J. W.; Tang, X.-J.; Peisach, J. *J. Am. Chem. Soc.* **1994**, *116*, 5250.

(11) Takahashi, S.; Sam, J. W.; Peisach, J.; Rousseau, D. L. *J. Am. Chem. Soc.* **1994**, *116*, 4408.

(12) Veselov, A.; Sun, H.; Sienkiewicz, A.; Taylor, H.; Burger, R. M.; Scholes, C. P. *J. Am. Chem. Soc.* **1995**, *117*, 7508.

(13) Westre, T. E.; Loeb, K. E.; Zaleski, J. M.; Hedman, B.; Hodgson, K. O.; Solomon, E. I. *J. Am. Chem. Soc.* **1995**, *117*, 1309.

(14) Neese, F.; Zaleski, J. M.; Loeb-Zaleski, K.; Solomon, E. I. *J. Am. Chem. Soc.* **2000**, *122*, 11703.

(15) The nature of the sixth ligand to iron(III) could not be determined (see ref 16), but is likely water ($x = 2$).[17]

(16) Zang, Y.; Kim, J.; Dong, Y.; Wilkinson, E. C.; Appelman, E. H.; Que, L., Jr. *J. Am. Chem. Soc.* **1997**, *119*, 4197.

(17) Lehnert, N.; Ho, R. Y. N.; Que, L., Jr.; Solomon, E. I. *J. Am. Chem. Soc.* **2001**, *123*, 8271−8290.

(18) Kim, J.; Larka, E.; Wilkinson, E. C.; Que, L., Jr. *Angew. Chem., Int. Ed. Engl.* **1995**, *34*, 2048.

10.1021/ja011450+ CCC: $20.00
Published on Web 12/19/2001

the O−O bond:[19−23]

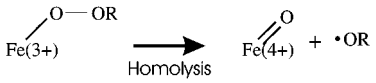

The alkoxo radical •OR is then capable of cleaving weak C−H bonds by abstracting an H-atom forming a C• radical that initiates radical chain reactions in the presence of O_2. This complex has been studied by different spectroscopies and density functional theory (DFT) calculations.[17] Its Raman spectrum shows three peaks at 796, 696, and 490 cm^{-1},[16] which have been assigned to the O−O (796 cm^{-1}) and the Fe−O (696 cm^{-1}) stretch and a combined O−C−C/C−C−C bend (490 cm^{-1}) that is mixed with ν(FeO).[17] The associated force constants indicate a strong Fe−O (force constant $k = 3.53$ mdyn/Å) and weak O−O bond ($k = 2.92$ mdyn/Å). The intense 600 nm absorption band of this complex has been assigned to an alkylperoxo to Fe(III) charge-transfer transition with the help of resonance Raman profiles. Using experimentally calibrated DFT calculations, the energetics of the homolytic cleavage of the O−O bond have been investigated.[17] Including solvent stabilization, the O−O homolysis is endothermic by only 15−20 kcal/mol. This is due to the large energetic stabilization of the Fe^{IV}═O product in the $S = 1$ and $S = 2$ spin states, which originates from the presence of two strong π and a strong σ bond between Fe(IV) and the oxo ligand. The endothermicity of this reaction is compensated for by the entropy gain upon splitting of the O−O bond and zero-field vibrational corrections, resulting in a thermoneutral reaction.

The analogous high-spin complex [Fe(6-Me_3TPA)(OH_x)(OO^tBu)]$^{x+}$ (**1**, $x = 1$ or 2)[16] shows very different spectroscopic properties compared to low-spin [Fe(TPA)(OH_x)(OO^tBu)]$^{x+}$. This compound is characterized by an intense absorption at 560 nm, Raman peaks at 876, 842, 637, and 469 cm^{-1}, and a rhombic ground state with effective g values of 4.3 derived from EPR spectroscopy. In addition, **1** has been characterized by electrospray ionization mass spectrometry,[16] which, however, does not identify the nature of the sixth ligand, presumably water or hydroxide (denoted as $(OH)_x$). In this study, the spectroscopic properties of the high-spin model complex **1** are determined using resonance Raman, UV−vis, magnetic circular dichroism (MCD), and variable-temperature variable-field (VTVH) MCD spectroscopies. The resonance Raman spectra of **1** have been analyzed in terms of normal coordinate analysis (NCA) and fully assigned. The force constants derived give insight into the strengths of the relevant bonds. Using polarizations derived from VTVH data together with resonance Raman profiles, the absorption and MCD spectra of **1** have been assigned. These results are correlated to DFT calculations in order to define the electronic structure of high-spin Fe(III)−alkylperoxo complexes. This enables a comparison with analogous low-spin Fe(III)−OO^tBu systems in terms of electronic structure and reactivity. The reaction coordinates of the homolytic cleavage of the O−O and the Fe−O bond have been evaluated for both the high-spin and low-spin complexes and have been correlated to their known reactivities.

(19) Kojima, T.; Leising, R. A.; Yan, S.; Que, L., Jr. *J. Am. Chem. Soc.* **1993**, *115*, 11328.
(20) Arends, I. W. C. E.; Ingold, K. U.; Wayner, D. D. M. *J. Am. Chem. Soc.* **1995**, *117*, 4710.
(21) Kim, J.; Harrison, R. G.; Kim, C.; Que, L., Jr. *J. Am. Chem. Soc.* **1996**, *118*, 4373−4379.
(22) MacFaul, P. A.; Arends, I. W. C. E.; Ingold, K. U.; Wayner, D. D. M. *J. Chem. Soc., Perkin Trans. 2* **1997**, 135.
(23) MacFaul, P. A.; Ingold, K. U.; Wayner, D. D. M.; Que, L., Jr. *J. Am. Chem. Soc.* **1997**, *119*, 10594.

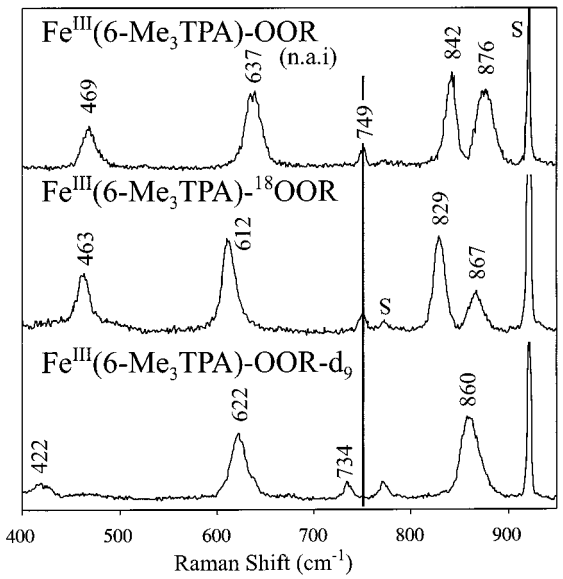

Figure 1. Resonance Raman spectra of **1**. From top to bottom: natural abundance isotopes (nai) spectrum; ^{18}O substituted ligand at the coordinating oxygen; ligand with fully deuterated *tert*-butyl group.

Experimental and Computational Procedures

See Supporting Information.

Results and Analysis

(A) Spectroscopy. (A.1) Resonance Raman Spectra and Vibrational Analysis. (A.1.1) Vibrational Assignment. Figure 1 shows the resonance Raman spectra of high-spin [Fe(6-Me_3-TPA)(OH_x)(OO^tBu)]$^{x+}$ (**1**) recorded at a laser wavelength of 514.5 nm exciting into the broad absorption band around 560 nm (vide infra). In the natural abundance isotopes (nai) spectrum (top panel), four peaks are found at 876, 842, 637, and 469 cm^{-1}. On ^{18}O substitution of the coordinating oxygen atom, these shift down to 867, 829, 612, and 463 cm^{-1} as shown in the middle panel. Importantly, whereas the two features at 876 and 842 cm^{-1} in the nai spectrum have about the same intensity, there is a redistribution of the resonance Raman intensity in the ^{18}O spectrum where the 829 cm^{-1} peak is more intense. This effect is even more pronounced in the bottom spectrum where the *tert*-butyl group is deuterated. Here, only one peak is observed at 860 cm^{-1}, indicating that the second vibration in this energy region has lost all of its intensity. The other two features at 637 and 469 cm^{-1} are shifted down to 622 and 422 cm^{-1} in the spectrum of the deuterated compound. In addition to these dominant peaks, a weak signal is observed in the nai spectrum at 749 cm^{-1} that does not show a significant shift on ^{18}O substitution but shifts down to 734 cm^{-1} on deuteration. These data have been reported.[16] On the basis of the analysis presented below, the 560 nm absorption is assigned as a CT transition from the alkylperoxo ligand to Fe(III). Therefore, the corresponding excited-state distortions should mainly occur along the O−O and Fe−O stretching coordinates, which would lead to two resonance enhanced vibrations in the Raman spectrum rather than the four intense peaks observed in the nai spectrum.

To understand the Raman spectra and extract force constants for estimating bond strengths, an NCA has been performed. Since the crystal structure of **1** is not known, a structure was estimated from density functional calculations that will be presented in part B. A simplified model of **1** where the three pyridine donors of the TPA ligand are substituted by NH_3 and

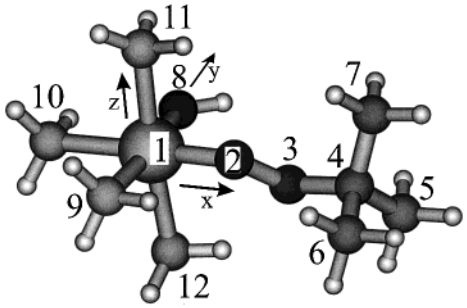

Figure 2. Optimized structure (B3LYP/LanL2DZ) of the simplified model **1̃a** in which the TPA ligand has been replaced by four ammonias and a hydroxide is used as the sixth ligand (see text). The coordinates of **1̃a** are given in the Table 4 of the Supporting Information. Important structural parameters (bond lengths in angstroms, angles in degrees): r(Fe−O) = 1.943; r(O−O) = 1.482; r(C−O) = 1.516; Fe−O−O: 111; C−O−O: 111; Fe−O−O−C: 175. The 12 heavy atoms of this system comprise the model used for NCA (**1̂a**) with the indicated numbering of the atoms.

a hydroxide molecule is used as sixth ligand (**1̃a**) was geometry optimized leading to the structure shown in Figure 2. For the NCA, all hydrogen atoms are neglected. The resulting model **1̂a** consists of the 12 heavy atoms of **1̃a** as indicated in Figure 2. Effective masses reflecting the TPA ligand are used for the nitrogens (M = 50 for N_9, M = 74 for N_{10}−N_{12}) of **1̂a** and a mass of 15 has been used for the carbons of the CH_3 groups (C_5−C_7). A further problem for the NCA is that while all vibrations of the Fe−O−O^{t}Bu unit are strongly coupled, the corresponding nondiagonal elements of the **f** matrix are not known. To solve this vibrational problem, a quantum chemistry assisted normal coordinate analysis (QCA-NCA)[24] has been performed. In this method, a simplified form of the quantum chemical derived force field of **1̃a** is used as a first approximation in the NCA, and then selected force constants are fitted to reproduce the experimental results. The force constants of the Fe−O−O^{t}Bu subunit of **1̂a** before (column labeled calc (x = 1)) and after (QCA-NCA (x = 1)) fitting to the experimental data are shown in Table 1 of the Supporting Information. The corresponding potential energy distributions (ped) from the QCA-NCA fit for the nai and the two isotope labeled species are given in Table 1 along with a comparison of the experimental and predicted vibrational energies.

The NCA unequivocally allows the assignment of the four peaks observed in the resonance Raman spectra of **1**. In the nai spectrum (Figure 1, top), the two features at 876 and 842 cm^{-1} correspond to the O−O stretch that is strongly mixed with the symmetric C−C stretch of the *tert*-butyl group. In the NCA simulation, the mode at higher energy has less ΔO−O character, as can be seen in the ped given in Table 1 (31 vs 48%). Since the intensities of the 876 and 842 cm^{-1} peaks are due to the ΔO−O admixture (vide infra), the experimental data indicate a more equal distribution of the O−O stretching character over the two normal modes. In addition, both have a small admixture of the C−O stretch (cf. Table 1). On ^{18}O substitution, these two modes shift down to 869 and 829 cm^{-1} accompanied by a redistribution of the resonance intensity. This is due to the fact that the ^{18}O labeling selectively shifts the O−O stretch to lower energy, which changes the composition of the two modes. As shown in Table 1, the vibration at higher energy now has predominantly C−C stretching character, whereas the more intense 829 cm^{-1} feature corresponds to the O−O stretch, and only the ΔO−O coordinate is resonance enhanced. The fact that the ΔC−C coordinate has no intrinsic resonance intensity is demonstrated by the bottom spectrum where the *tert*-butyl group is deuterated. Here, the C−C stretch is shifted down in energy which strongly reduces mode mixing with the O−O stretch, and hence, only one peak is observed at 860 cm^{-1}. In the NCA, ν_s(CC) appears at 817 cm^{-1} (with 10% ΔO−O admixture) and the peak at 860 cm^{-1} is a fairly clean O−O stretch (cf . Table 1). Therefore, the vibrational frequency of 860 cm^{-1} corresponds to the spectral position of ν(OO) when mode mixing is small. The observed shifts on isotope substitution are well-reproduced in the NCA (cf. Table 1). Note that a small peak appears in the nai spectrum at 749 cm^{-1} which is best assigned as the C−O stretch ν(CO).

At lower energy, the peak at 637 cm^{-1} in the nai spectrum is assigned to the Fe−O stretch ν(FeO) and the feature at 469 cm^{-1} to a combined δ(OCC)/δ(CCC) bending vibration that has a large ν(FeO) admixture, which is the source of the resonance intensity of this mode. In the NCA simulation, there are three δ(OCC)/δ(CCC) bends in the energy region between 470 and 528 cm^{-1} (in square brackets in Table 1), whereas in the corresponding DFT calculation the bends at highest energy are located around 450 cm^{-1} (included at the bottom of each simulation in Table 1) using the same set of diagonal force constants (D1−D3 and E1−E3; cf. Table 1 of the Supporting Information). This is due to the fact that the O−C−C and C−C−C bends are also mixed with C−C−H bends. Since the hydrogens of the *tert*-butyl group have been omitted in the NCA simulation, the δ(OCC)/δ(CCC) bends cannot accurately be described in the NCA and hence, they have not been included in the fit (only nondiagonal elements K3 and K4 were allowed to vary; cf. Table 1 of the Supporting Information). In the DFT calculation, only one δ(OCC)/δ(CCC) bend at 447 cm^{-1} shows strong mixing with ν(FeO) in agreement with experiment, where only one of these bends has resonance intensity. Analysis of the resonance Raman profiles shows that the calculated ΔFe−O contribution to the 447 cm^{-1} bend of 19% (cf. Table 1) is an underestimate (from the Heller analysis in section A.2, the admixture is about 46%). This assignment is in good agreement with the NCA of the vibrational data of the related low-spin [Fe(TPA)(OH$_x$)(OO^{t}Bu)]$^{x+}$ complex.[17] In the ^{18}O labeled spectrum, ν(FeO) shifts to 612 cm^{-1}, and the δ(OCC)/δ(CCC) bend is located at 463 cm^{-1}. On deuteration of the *tert*-butyl group, ν(FeO) is found at 622 cm^{-1}, whereas the bend at 469 cm^{-1} shows a large shift of −47 cm^{-1} to +422 cm^{-1} (cf. Figure 1). This is in good agreement with the calculated shift of the 447 cm^{-1} mode from DFT (cf. Table 1) and confirms the assignment of the 469 cm^{-1} peak as a δ(OCC)/δ(CCC) bend. The fact that this mode loses about half of its intensity on deuteration is due to the increased energy separation to ν(FeO) which decreases mode mixing. This is not reproduced well in the DFT calculation due to the underestimate of mode mixing of the δ(OCC)/δ(CCC) bend with ν(Fe−O) and the fact that the Fe−O stretch is calculated at too low an energy (590 cm^{-1} compared to the experimental value of 637 cm^{-1}).

(A.1.2) Analysis of Force Constants. Table 1 of the Supporting Information gives a list of the force constants of the Fe−O−O−C(C_3) subunit of **1̂a** (for the complete **f** matrix see Table 6 of the Supporting Information). The starting point for the NCA are the calculated force constants for model **1̃a** given in Table 1 of the Supporting Information, middle (calc: x = 1). The final values obtained after fitting to the experimental data are shown in Table 1 of the Supporting Information, right (QCA-NCA: x = 1). For the diagonal elements, the changes are within ±0.9 and for nondiagonal elements within ±0.5.

(24) Lehnert, N.; Tuczek, F. *Inorg. Chem.* **1999**, 1659.

Table 1. Comparison of Experimental and QCA-NCA (and DFT) Frequencies and Potential Energy Distributions[a]

			potential energy distribution							
expt freq		QCA-NCA (DFT)	ΔFe−O	ΔO−O	ΔC−O	ΔC−C	∠Fe−O−O	∠C−O−O	∠O−C−C	∠C−C−C
					$Fe-^{16}O-^{16}O-C(^{15}C)_3$ (nai)					
876		875	1	31	7	47	1	2	7	4
842		842	1	48	13	27	1	2	6	2
(749 ?)		738	8	0	41	10	16	21	2	1
637		633	47	0	26	4	2	7	9	4
		[528][b]	22	0	2	3	1	1	41	27
469		[518][b]	1	0	0	9	0	0	56	28
		[478][b]	8	4	1	6	19	0	16	43
	DFT	450[c]	8	0	1	3	0	0	46	23
		447[c]	19	0	1	3	0	1	37	24
					$Fe-^{18}O-^{16}O-C(^{15}C)_3$					
867		869	0	12	11	62	0	1	8	5
829		829	1	64	10	13	1	4	6	1
(749 ?)		732	5	0	47	10	14	19	3	1
612		615	45	1	20	4	3	9	11	6
		[525][b]	28	1	1	3	1	1	38	25
463		[517][b]	2	0	0	8	0	0	55	28
		[474][b]	9	5	1	5	17	0	13	46
	DFT	449[c]	2	0	0	4	0	0	52	23
		443[c]	22	0	1	1	0	1	21	16
					$Fe-^{16}O-^{16}O-C(^{18}C)_3$					
860		860	2	75	0	10	2	4	6	1
−		817	0	10	29	46	0	0	9	6
(734 ?)		724	11	0	30	16	18	24	1	0
622		623	54	1	23	7	2	5	5	2
		[506][b]	16	0	4	6	1	2	41	27
422		[490][b]	0	0	0	10	0	0	60	21
		[453][b]	7	1	0	5	12	0	13	26
	DFT	400[c]	5	0	1	2	1	1	51	12
		394[c]	18	1	3	2	1	3	32	15

[a] For $Fe-^{18}O-^{18}O-C(^{15}C)_3$, the following energies are predicted by NCA (cm^{-1}; in brackets the type of stretching vibration): 866 (C−C)/803 (O−O)/707 (C−O)/613 (Fe−O)/[519, 510, 473, 388]. [b] Values in square brackets: not fit; this region is cleaned up by interaction of the O−C−C/C−C−C bends with C−C−H bends which causes the δ(OCC)/δ(CCC) modes to shift to lower energy as can be seen from the DFT results. [c] The two O−C−C/C−C−C bends at highest energy in the DFT calculation of **1̃**. The remaining bends at lower energy do not show any admixture from ΔFe−O and ΔO−O.

Compared to the DFT calculation on **1̃a**, the largest changes occur for the Fe−O, C−O and Fe−O−O diagonal force constants and the nondiagonal elements between the Fe−O−O bend and the Fe−O and O−O stretches. Complex **1** has a medium strong Fe−O bond with a force constant of 2.87 mdyn/Å and a strong O−O bond with $k = 3.55$ mdyn/Å. The Fe−O−O and C−O−O bend force constants are of about the same magnitude ($k = 1.34$ vs 1.39 mdyn·Å). Note that the final force field for **1̂a** in Table 1 of the Supporting Information, right, has many similarities to the force field obtained from QCA-NCA for low-spin $[Fe(TPA)(OH_x)(OO^tBu)]^{x+}$.[17] The striking differences are that complex **1** has a weaker Fe−O (k(hs) = 2.87 mdyn/Å vs k(ls) = 3.53 mdyn·Å) and a stronger O−O bond (k(hs) = 3.55 mdyn/Å vs k(ls) = 2.92 mdyn/Å).

(A.2) UV−Vis Absorption, MCD, and Resonance Raman Profiles. The absorption spectrum of **1** is shown in Figure 3, top. One broad absorption band is observed in the visible region around 17 900 cm^{-1} (560 nm; $\epsilon = 2000$ M^{-1} cm^{-1}). The intensity then rapidly increases to higher energy, but no further distinct absorption band can be identified. The MCD spectrum in Figure 3, bottom, resolves two more features in the UV region at roughly 28 000 and 32 000 cm^{-1}. To identify additional bands in the MCD spectrum, VTVH MCD data have been recorded at a number of different wavelengths that are marked with arrows through the spectrum in Figure 3, bottom. The data recorded at 16 400, 18 200, and 20 000 cm^{-1} show about the same nesting behavior of the VTVH curves, which indicates that the broad absorption around 17 900 cm^{-1} is either due to a single electronic transition or several transitions that are polarized along the same molecular axis (see refs 25 and 26). VTVH isotherms recorded at 18 200 cm^{-1} (550 nm) in the center of band 1 are shown in Figure 4. To higher energy, a different nesting behavior is observed at 22 000 and 25 000 cm^{-1}, indicating that an additional electronic transition is located in this energy region. Figure 4 shows the data recorded at 25 000 cm^{-1}, which are very similar to the isotherms obtained at 22 000 cm^{-1}. For the band at 28 000 cm^{-1}, the VTVH curves measured at 27 800 cm^{-1} show only very little nesting (cf. Figure 4). Finally, VTVH isotherms recorded at 31 250 cm^{-1} indicate the presence of another transition in this energy region. Thus, the absorption and MCD spectra of **1** must be fit with a minimum of four bands. Table 2 gives the resulting parameters of the four fitted Gaussians that are shown as dashed lines in Figure 3. The position of band 2 is not well-defined from the VTVH data and can be shifted within the 24 000−25 000 cm^{-1} energy region without affecting the overall quality of the fit. The position of this band strongly influences its fit intensity, which is therefore also uncertain.

Figure 3, top, also contains the resonance Raman profiles for the modes at 876 and 842 cm^{-1} with ν(OO) character, the Fe−O stretch (637 cm^{-1}), and the δ(OCC)/δ(CCC) bend at 469 cm^{-1}, which has a large ν(FeO) admixture (vide supra). All four vibrations are clearly resonance enhanced with respect to the broad 560 nm absorption feature. Therefore, the excited state corresponding to this electronic transition is mostly displaced along the ΔFe−O and ΔO−O stretching coordinates relative

(25) Neese, F.; Solomon, E. I. *Inorg. Chem.* **1999**, *38*, 1847.
(26) Lehnert, N.; DeBeer George, S.; Solomon, E. I. *Curr. Opin. Chem. Biol.* **2001**, *5*, 173.

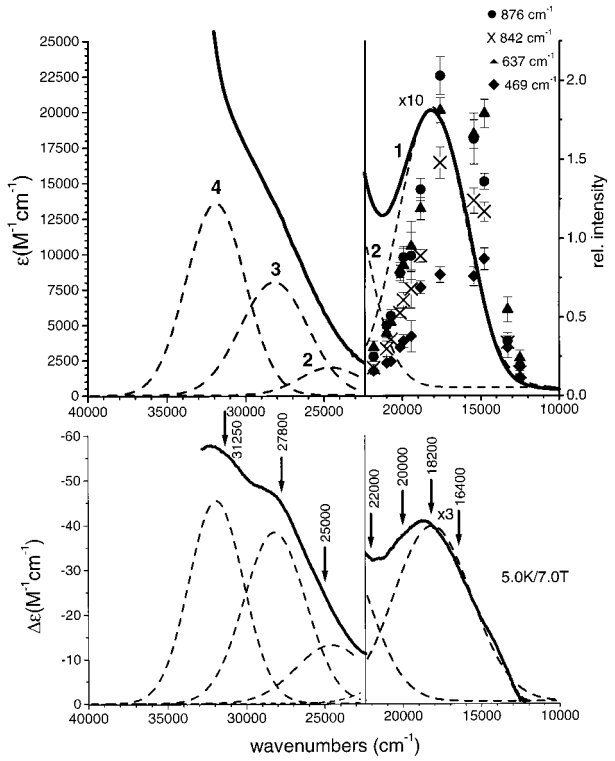

Figure 3. UV−vis (top) and MCD spectra (bottom; recorded at 5 K and 7 T) of **1** together with a correlated Gaussian fit (bands 1−4). The low-energy range of the UV−vis spectrum (top, right) is enlarged by a factor of 10 (ϵ = 2000 M^{-1} cm^{-1}) and the corresponding range of the MCD spectrum by a factor of 3 (bottom, right). Arrows in the MCD spectrum indicate energies at which VTVH data were recorded (cm^{-1}). The UV−vis panel on the top, right, also contains the resonance Raman profiles of ν(FeO) (▲, 637 cm^{-1}), ν(OO) (●, 876 cm^{-1}; ×, 842 cm^{-1}) and δ(OCC/CCC) (◆, 469 cm^{-1}).

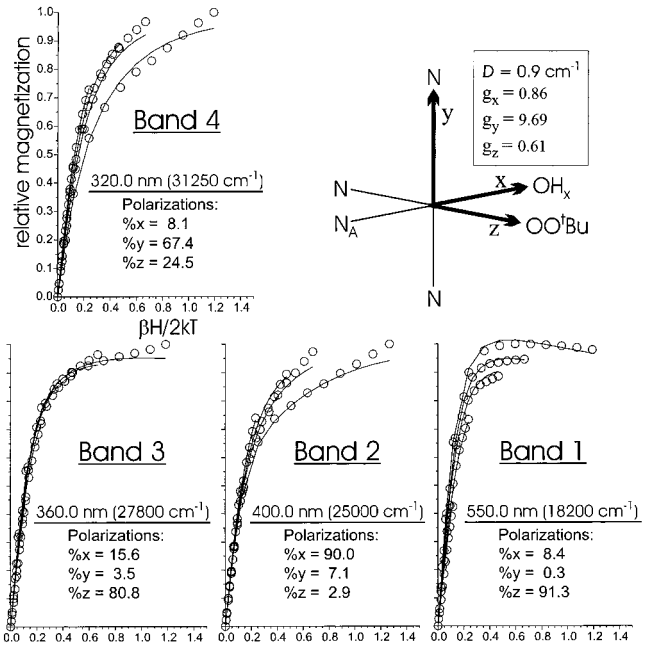

Figure 4. VTVH MCD data of bands 1−4 (cf. Figure 3). On the top, right, a simplified sketch of **1** is shown where the four "N" ligands represent the TPA ligand ("N_A" is the amine donor) and "OH_x" is hydroxide/water (see text). The analysis of the VTVH data leads to the given orientation of the ZFS tensor in the molecular framework. The insert gives the obtained *D* value from the fit and the effective *g* values of the lowest doublet.

to the ground state. Hence, the 560 nm absorption (band 1) corresponds to a charge-transfer transition between the alkyl-

Table 2. Result of the Correlated Gaussian Fit of the Absorption and MCD Spectrum

band	ν_{max} (cm^{-1})	ϵ_{max} (M^{-1} cm^{-1})	$\Delta\epsilon_{max}$ (M^{-1} cm^{-1})	f^a	$\lvert\Delta\epsilon/\epsilon\rvert$
1	18 123	2022	+13	0.047	0.007
2	24 572[b]	1975	+13	0.043	0.007
3	28 185	8020	+38	0.187	0.005
4	31 911[b]	13597	+45	0.261	0.003

[a] *f*: Oscillator strength. [b] Position of absorption/MCD band is not clearly determined from the spectroscopic data. The fit presented here is therefore only of tentative character.

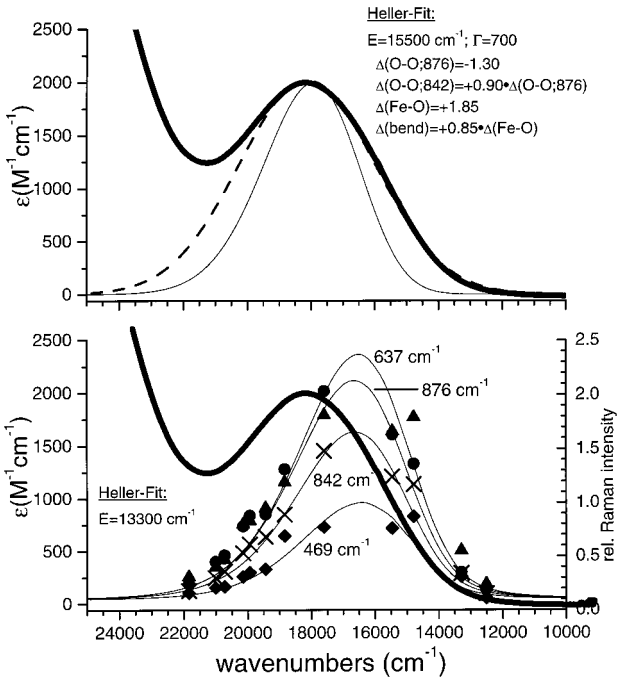

Figure 5. Heller fit of the absorption spectrum (top; the dashed line is band 1 from the fit of the absorption and MCD data) and the resonance Raman profiles (bottom) of ν(FeO) (▲, 637 cm^{-1}), ν(OO) (●, 876 cm^{-1}; ×, 842 cm^{-1}) and δ(OCC)/δ(CCC) (◆, 469 cm^{-1}). The solid line represents the UV−vis spectrum from Figure 3. The parameters are: the energy of the electronic origin *E* (band 1); dimensionless displacements Δ for the four normal modes; intrinsic line width Γ. For the fit of the absorption spectrum, the energy of the electronic origin *E* has been shifted.

peroxo ligand and high-spin Fe(III). Close examination of the resonance profiles shown in Figure 3, top, and Figure 5, bottom, reveals a small reproducible shoulder on the high-energy side of each of the three more intense profiles. This indicates that there could be a second transition under the broad absorption band at 560 nm, which is weak compared to band 1.

(A.2.1) Analysis of the VTVH MCD Data. Figure 4 gives the VTVH data (open circles) together with best fits (solid lines) of the absorption bands 1−4 which result from the correlated Gaussian fit of the UV−vis and MCD spectra (cf. Figure 3). For band 1 at the low-energy side of the spectrum, a very good fit of the VTVH isotherms (measured at 550 nm) has been obtained. This transition is dominantly *z* polarized, and, since this band has been assigned to an alkylperoxo to Fe(III) charge transfer, the *z* axis of the ZFS tensor must be aligned with the Fe−OO^{t}Bu bond, as shown in Figure 4, top right. Note that the polarization directions are relative to the orientation of the **D** tensor.[25,26] For band 2, a completely different behavior of the VTVH isotherms is observed, as shown in Figure 4. The data recorded at 400 nm are strongly polarized along the *x* direction. Since this transition is at too low an energy to be a pyridine to Fe(III) charge transfer, it is tentatively assigned as either a water

or hydroxide to Fe(III) CT (see Introduction), where the low energy of about 24 000−25 000 cm^{-1} of band 2 argues for hydroxide rather than water. The VTVH data for band 3 (recorded at 360 nm) again show a different type of behavior compared to that of bands 1 and 2. Here, almost no nesting of the VTVH curves is observed. This transition is mostly *z* polarized like band 1, and hence, it could either be a pyridine to Fe(III) or alkylperoxo to Fe(III) charge transfer. However, the intensity and position of this band argue for a transition originating from pyridine. This derives from CT energies estimated from DFT calculations on $\tilde{\mathbf{1}}\mathbf{a}$ (vide infra). Since this band is *z* polarized, this is an indication that the ligand trans to alkylperoxide is actually a pyridine and not the amine donor of the TPA ligand. Hence, the amine donor (N_A) must be located in the position trans to the water/hydroxide ligand of **1,** as indicated in Figure 4, top right. For band 4, the VTVH data recorded at 320 nm have larger error bars compared to the other data sets due to the strong absorbance of the sample in the UV region, which limits the accuracy of the fit. This band is 67% *y* and 25% *z* polarized and can be assigned to a pyridine to Fe(III) CT transition.

(A.2.2) Heller Analysis of the Resonance Raman Profiles and Nature of the Excited State. Analysis of the resonance Raman profiles of the four vibrations corresponding to ν(OO) (876/842 cm^{-1}), ν(FeO) (637 cm^{-1}), and the OCC/CCC bend (469 cm^{-1}) with time-dependent Heller theory[27] offers further insight into the nature of the broad absorption band at 560 nm. As shown in Figure 5, bottom, all four profiles are symmetric and their shapes and relative intensities are reproduced well when fitted with one electronic transition. The electronic origin of band 1 as well as the dimensionless displacements for the different normal modes from the Heller simulation are given in Figure 5. Note that the Heller analysis does not give the sign of Δ; this information is obtained from the assignment of the CT transition (cf. section B). Since the 469 cm^{-1} bending vibration gains its intensity by mixing with ν(Fe−O), the displacement of this mode is related to Δ(Fe−O). The coefficient of 0.85 corresponds to an admixture of about 46% ν(Fe−O) into δ(OCC)/δ(CCC) and is in good agreement with the estimated coefficient of 0.93 calculated with the preresonance formula:[27d,28,29]

$$\frac{I(\text{Fe}-\text{O})}{I(\text{bend})} = \left(\frac{\Delta(\text{Fe}-\text{O})\cdot\nu(\text{Fe}-\text{O})}{\Delta(\text{bend})\cdot\nu(\text{bend})}\right)^2$$

where *I* is the integrated resonance Raman peak intensity at a specific excitation wavelength and ν is the vibrational energy.

The Heller fit of absorption band 1 is shown in Figure 5, top,[30] together with the UV−vis spectrum of complex **1**. The simulated absorption band from the Heller analysis assuming one transition (solid line in Figure 5, top) has a distinctly smaller half-width than the Gaussian fit (dashed line; corresponds to band 1 in Figure 3), while the shapes of the resonance profiles are reproduced well in the fit (cf. Figure 5, bottom). This was not the case for the low-spin $[Fe(TPA)(OH_x)(OO^tBu)]^{x+}$ complex,[17] where both the simulated absorption and profile bandwidths were in very good agreement with experiment. This difference suggests the presence of an additional absorption band under the broad 560 nm feature which is weak in absorption, polarized along the Fe−O bond (from the VTVH MCD) and where the corresponding excited state is displaced along the Fe−O and O−O bonds (from the resonance Raman profiles). This additional band would therefore correspond to an overlap-forbidden (and hence weak) CT transition between alkylperoxide and iron(III).

From the dimensionless displacements Δ, the Huang−Rhys parameter S_p^J for excited state $|J\rangle$ and normal mode *p* can be calculated: $S_p^J = 1/2(\Delta_p{}^J)^2$. Absolute displacements along the internal coordinate *i* (in Å) can be obtained with the formula[27c]

$$\Delta r_i(\text{Å}) = 5.8065\sum_p l_{p,i}\frac{\Delta_p}{\sqrt{\nu_p}} \qquad (1)$$

with $l_{p,i}$ being the eigenvector from NCA for normal mode *p*, Δ_p is its dimensionless displacement, and ν_p the vibrational energy (in cm^{-1}). For bond distances, the eigenvector $l_{p,i}$ is directly related to the change in bond length, and hence, eq 1 gives the absolute displacement along the bond. Table 2 of the Supporting Information gives the resulting excited-state distortions relative to the ground state obtained from the Heller analysis of band 1 using the eigenvectors from QCA-NCA. The excited state is mainly displaced along the O−O and Fe−O bonds in accordance with the assignment of the 560 nm absorption to an alkylperoxo to Fe(III) CT transition. Note that the calculated Fe−O displacement in Table 2 of the Supporting Information is an underestimate since the contribution from the ΔFe−O coordinate that is mixed into the 469 cm^{-1} vibration is not included. The calculated distortions along the angle bending coordinates are very small and, hence, correspond to negligible displacements when transformed from angstroms into degrees.[17] The calculated values for ΔO−O and ΔC−O in Table 2 of the Supporting Information are in very good agreement with the displacements obtained for low-spin $[Fe(TPA)(OH_x)(OO^tBu)]^{x+}$. On the other hand, ΔFe−O is smaller for **1** which is in accordance with the additional Fe−O displacement observed for the low-spin complex due to the CI mixing of the CT with a ligand field excited state.[17]

(A.3) Donor Strength of the Charge-Transfer State. The above studies have rigorously defined the alkylperoxo to Fe(III) CT transition energy and intensity which can now be related to the donor strength of this bond. Using the formalism in ref 31, the donor strength of a ligand is approximately given by the equation

$$(C_{\pi^*}^M)^2 = (9.22\times10^{-2}\,[\text{Å}])\sum_i \frac{f_i}{\nu_i|\mathbf{r}|^2}$$

with *f* being the oscillator strength and ν the frequency of the *i*th charge-transfer band and **r** is the transition vector that coincides with the Fe−O bond and can be set to the Fe−O bond length. This equation relates the metal d orbital contributions to the ligand donor orbitals and therefore the donor strength of the metal−ligand bond to the intensity of the resulting CT transition. The donor strength is calibrated relative to the value obtained for an end-on copper−peroxide monomer which has

(27) (a) Lee, S. Y.; Heller, E. J. *J. Chem. Phys.* **1979**, *71*, 4777. (b) Tannor, D. J.; Heller, E. J. *J. Chem. Phys.* **1982**, *77*, 202. (c) Myers, A. B.; Mathies, R. A. In *Resonance Raman Intensities: A Probe of Excited-State Structure and Dynamics*; Spiro, T. G., Ed.; Wiley: New York, 1987; Vol. 2, pp 1−58 (d) Zink, J. I.; Shin, K.-S. K. *Adv. Photochem.* **1991**, *16*, 119.

(28) Tang, J., Albrecht, A. C., Szymanski, H. A., Eds. Plenum Press: New York, 1970; Vol. 2, pp 33−68.

(29) Warshel, A.; Dauber, P. *J. Chem. Phys.* **1977**, *66*, 5477.

(30) Note that the electronic origin of band 1 is shifted to higher energy in the fit of the absorption spectrum compared to the fit of the resonance Raman profiles. This is due to the different experimental conditions required by the data collection (solution at −40 °C vs frozen solution (77 K); cf. Experimental Section). All other parameters (cf. Figure 5) are identical.

(31) Baldwin, M. J.; Root, D. E.; Pate, J. E.; Fujisawa, K.; Kitajima, N.; Solomon, E. I. *J. Am. Chem. Soc.* **1992**, *114*, 10421.

Table 3. Comparison of Relative Donor Strengths and M−O Force Constants of Cu− and Fe−Peroxo Complexes

complex	$\pi^* \rightarrow$ d CT (cm^{-1})	donor strength $(C^M_{\pi^*})^2$ ratio[a]	ν_{M-O} (cm^{-1})	k_{M-O}[b] (mdyn/Å)	ν_{O-O} (cm^{-1})	k_{O-O}[b] (mdyn/Å)	ref
Cu end-on monomer	19 880	1.0	488	1.94 (1.89)	803	2.90 (2.86)	47
Cu end-on dimer	19 085	1.9	561	1.99 (1.94)	832	3.17 (3.10)	48
Cu side-on dimer	26 570	3.7	572	1.54 (1.42)	763	2.43 (2.43)	31
Fe(III) end-on dimer	14 620 24 650 26 200	1.4−1.8	421	1.99	876	3.07	49
L3CuOOCm[c]	16 590	1.1	645	3.03	843/809	3.22	39
L3CuOOH	16 560	>0.3	624	2.94	843	3.51	
side-on hs-Fe(EDTA)O_2	18 800 21 700 25 250 31 050	0.7−1.2	459	1.56	816	3.02	50
ls-Fe(TPA)OO^{t}Bu	16 000 17 364	0.5	696	3.53	796	2.92	17
hs-Fe(6−Me_3TPA)OO^{t}Bu	18 123	0.5	637	2.87	860[d]	3.55	*e*

[a] Corresponds to the charge donation of peroxide to the metal relative to the end-on monomer (set to 1.0). [b] Urey−Bradley force constants in parentheses; cf. ref 39. [c] Cm = Cumene [d] The O−O stretching frequency in the deuterated compound where mode mixing with ν_s(CC) is small. [e] This work.

Table 4. Calculated (B3LYP/LanL2DZ) Geometries and Properties of Three Models for High-Spin [Fe(TPA)(OH_x)(OO^{t}Bu)]$^{x+}$ (**1**)[a]

	geometric parameters[b]				
molecule	*r*(Fe−O)	*r*(O−O)	*r*(C−O)	*r*(Fe−OH_x)	*r*(Fe−N)[c]
hs-[Fe(NH_3)$_4$(OH_2)(OO^{t}Bu)]$^{2+}$ (**$\tilde{1}$**)	2.087	1.394	1.608	2.165	2.235
hs-[Fe(Ime)$_3$(NH_3)(OH_2)(OO^{t}Bu)]$^{2+}$	2.072	1.399	1.595	2.147	2.196[d]
hs-[Fe(NH_3)$_4$(OH)(OO^{t}Bu)]$^+$ (**$\tilde{1}$a**)	1.943	1.482	1.516	1.871	2.247
[Fe(NH_3)$_4$(OH)(OO^{t}Bu)]$^+$ (S = 3/2)	1.845	1.504	1.513	1.826	2.203

	spin densities				
molecule	Fe	O2	O3	C_{3t}	O(H_x)[e]
hs-[Fe(NH_3)$_4$(OH_2)(OO^{t}Bu)]$^{2+}$ (**$\tilde{1}$**)	+3.87	+0.58	+0.31	0.01	+0.03
hs-[Fe(Ime)$_3$(NH_3)(OH_2)(OO^{t}Bu)]$^{2+}$	+3.88	+0.58	+0.28	0.01	+0.04
hs-[Fe(NH_3)$_4$(OH)(OO^{t}Bu)]$^+$ (**$\tilde{1}$a**)	+4.00	+0.35	+0.05	0	+0.33
[Fe(NH_3)$_4$(OH)(OO^{t}Bu)]$^+$ (S = 3/2)	+2.72	+0.08	+0.01	0	+0.08

[a] Ime = imine ligand H−N=CH_2 as a model for pyridine. [b] Bond lengths in angstroms. [c] Averaged over all Fe−N bonds. [d] For the model with three imines, the average Fe−N_{IM} bond length is very similar to Fe−N_{AM}. [e] Spin density on the oxygen of the water or hydroxo ligand, respectively. Mulliken charges of the different complexes are given in Table 3 of the Supporting Information.

been set to a donor strength of 1.0. From Table 3, the relative donor strength of the alkylperoxo to Fe(III) charge-transfer transition of complex **1** (corresponding to band 1) is about 0.5 and, therefore, of the same magnitude as in low-spin [Fe(TPA)(OH_x)(OO^{t}Bu)]$^{x+}$. In comparison, this number is significantly lower than the relative donor strength of the visible absorption band in the corresponding copper complex [(L3)Cu(OOCm)] as shown in Table 3. To define the electronic structure of **1** in relation to these experimental results, DFT calculations have been performed which are presented below.

(B) Density Functional Calculations. (B.1) Geometry and Evaluation Based on Spectroscopic Features. The crystal structure of **1** is not known, and the sixth ligand to iron(III) could either be water or hydroxide. To estimate a reasonable structure for **1**, ammonia ligands have been applied as a model for the TPA ligand. This type of approximation has been shown to be valid in a number of related studies. A corresponding model system for low-spin [Fe(TPA)(OH_x)(OO^{t}Bu)]$^{x+}$ has been shown to reproduce spectral properties in good agreement with experiment.[17] Calculations on a related low-spin Fe(III)−hydroperoxo complex have led to comparable descriptions for the Fe(III)−OOH subunit when ammonias, imines (HN=CH_2), or the full ligand was used.[32a] In addition, calculations on the reaction coordinate of the enzyme isopenicillin N synthase by Siegbahn et al. have shown that the reaction energies are comparable whether imidazoles or ammonias were applied.[32b] On the basis of this, two possible model systems for **1**, high-spin [Fe(NH_3)$_4$(OH_2)(OO^{t}Bu)]$^{2+}$ (**$\tilde{1}$**) and high-spin [Fe(NH_3)$_4$(OH)(OO^{t}Bu)]$^+$ (**$\tilde{1}$a**), have been fully geometry optimized. Table 4 gives the resulting geometric parameters from the DFT calculations. Complex **$\tilde{1}$** has a long Fe−O bond of 2.087 Å and a very short O−O bond of 1.394 Å and correspondingly, as shown in Table 5, a low ν(FeO) at 366 cm^{-1} and a high ν(OO) at 998 cm^{-1}. In fact, this corresponds to an Fe(II)−alkylperoxyl complex where the alkylperoxo ligand is oxidized by one electron and the metal is reduced to Fe(II). Replacing three of the ammonia ligands in **$\tilde{1}$** with imines ("Ime", HN=CH_2; cf. Figure 4 of the Supporting Information), which better model the pyridine donors in the TPA ligand of **1**, does not change this Fe(II)−alkylperoxyl bonding description (cf. Table 4). Alternatively, model **$\tilde{1}$a** is in agreement with the oxidation state of **1**. Here, the Fe−O bond length is calculated to be 1.943 Å and the O−O distance is 1.482 Å. This is in agreement with the crystal structure of [Cu(L_1)(OOCm)][33] and the calculated structure of low-spin [Fe(TPA)(OH_2)(OO^{t}Bu)]$^{2+}$.[17] Compared to the low-spin Fe(III) complex, the much larger Fe−O distance in the case of **$\tilde{1}$a** (1.943 Å vs 1.818 Å in ls) is due to the high-

(32) (a) Lehnert, N.; Neese, F.; Ho, R. Y. N.; Que, L., Jr.; Solomon, E. I. Submitted for publication. (b) Wirstam, M.; Siegbahn, P. E. M. *J. Am. Chem. Soc.* **2000**, *122*, 8539.

(33) Kitajima, N.; Katayama, T.; Fujisawa, K.; Iwata, Y.; Moro-oka, Y. *J. Am. Chem. Soc.* **1993**, *115*, 7872.

Table 5. Calculated (B3LYP/LanL2DZ) and Experimental Frequencies and Force Constants

	force constant (mdyn/Å)			freq (cm^{-1})		
calcd/exptl	FeO	OO	CO	FeO	OO	ref
calcd: ^{t}BuOOH		3.92	3.81		900	
expt: ^{t}BuOOH− NCA:CH_3OOCH_3[a]		4.07	4.56		884 (?)	17
calcd: ^{t}BuOO$^-$		3.13	4.46		810	
calcd: ls-$[Fe(NH_3)_4(OH_2)(OO^tBu)]^{2+}$	3.38	3.39	2.43	626	843	
calcd: ls-$[Fe(NH_3)_4(OH)(OO^tBu)]^{+}$	2.89	3.47	3.46	625[b]	877	17
NCA: ls-$[Fe(TPA)(OH_x)(OO^tBu)]^{x+}$	3.53	2.92	2.83	696	796	
calcd: hs-$[Fe(NH_3)_4(OH_2)(OO^tBu)]^{2+}$	0.74	5.09	1.87	366	998	
calcd: hs-$[Fe(NH_3)_4(OH)(OO^tBu)]^{+}$	2.10	3.69	3.35	590	876	*c*
NCA: hs-$[Fe(TPA)(OH_x)(OO^tBu)]^{x+}$	2.87	3.55	2.45	637	860[d]	

[a] The IR spectrum (gas phase) of ^{t}BuOOH in ref 51 has not been assigned; the O−O and C−O force constants have been calculated for CH_3OOCH_3,[52] where ν(OO) = 779 cm^{-1}. [b] Raised in energy by interaction with the Fe−OH stretch (ν(Fe−OH) = 575 cm^{-1}; k = 2.623 mdyn/Å). [c] This work. [d] The O−O stretching frequency in the deuterated compound where mode mixing with ν_s(CC) is small.

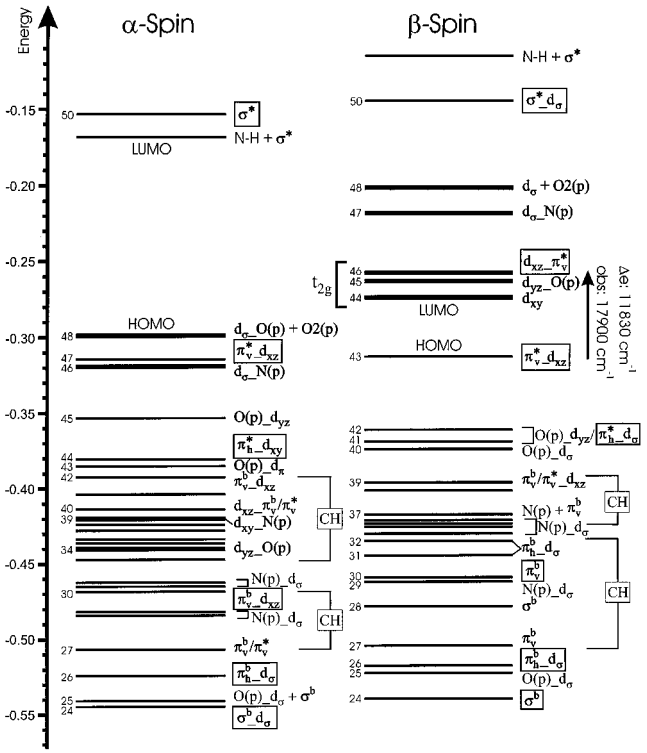

Figure 6. Molecular orbital diagram of **1̃a** (in the coordinate system given in Figure 2) calculated with B88P86/triple-ζ basis. The nomenclature "*a*_*b*" indicates that orbital *a* interacts with *b* and that *a* has a larger contribution to the resulting MO. Important MOs corresponding to the donor orbitals of the alkylperoxo ligand are marked with a box. Thick lines correspond to MOs with large iron d contributions (> 50%).

spin state of Fe(III) which leads to reduced σ bonding and increased bond lengths (vide infra). In addition, the ν(FeO) and ν(OO) vibrational frequencies and corresponding force constants of **1̃a** are in agreement with the experimental data on **1**. Some quantitative deviations, especially for the Fe−O force constant (experimental, 2.87 mdyn/Å; calculated, 2.10 mdyn/Å; cf. Table 5), are present which will impact the calculated molecular orbital (MO) diagram of **1̃a**.

(B.2) Description of the Electronic Structure of 1. Figure 6 shows the spin-unrestricted molecular orbital diagram of complex **1** (calculated for **1̃a** using the B88P86 functional and a Slater-type triple-ζ (valence) basis set; see Experimental Section). In an octahedral environment, the five d orbitals of iron split into 3-fold (t_{2g}) and 2-fold (e_g) degenerate sets. The three t_{2g} orbitals (d_{xy}, d_{yz}, d_{xz}) undergo π interactions with ligands, whereas the e_g functions (d_{z^2}, $d_{x^2-y^2}$) mediate σ bonds. Due to the $[t_{2g}]^3[e_g]^2$ configuration of high-spin iron(III), each d orbital is singly occupied leading to a $^6A_1$ ground state with maximum multiplicity. In a spin-unrestricted formalism, all five α-spin d orbitals are occupied, whereas the five β-spin functions are empty. The free ^{t}BuOO$^-$ ligand has several π and σ donor orbitals that could potentially be involved in bonding interactions with the Fe(III) center (see Experimental Section). Since alkylperoxide acts as a donor ligand, only the unoccupied β-spin d orbitals contribute to net bonding. Hence, the β MO diagram is discussed below. Note that the HOMO of complex **1** is an α-spin e_g orbital as shown in Figure 6.

The HOMO of the ^{t}BuOO$^-$ ligand, π_v^*, forms a π bond with the β-d_{xz} orbital of iron (in the coordinate system given in Figure 2). The bonding combination, π_v^*_d_{xz} ($\beta\langle 43\rangle$),[34] has 28% iron contribution as given in Table 6, which corresponds to a very covalent bond. A contour plot of this MO is shown in Figure 7. The antibonding combination of these orbitals, d_{xz}_π_v^* ($\beta\langle 46\rangle$), is unoccupied and distinctly shifted to higher energy-compared to the almost nonbonding t_{2g} function β-d_{xy} ($\beta\langle 44\rangle$) in Figure 6, right, which is also an indication of the strength of this interaction. The orbital d_{xz}_π_v^* has 69% metal character and a corresponding π_v^* covalency of 24% (cf. Table 6). Together with the resonance Raman results (vide supra), the intense absorption around 17 900 cm^{-1} is assigned as an alkylperoxo to Fe(III) (π_v^*_d_{xz} to d_{xz}_π_v^*) CT transition corresponding to an Fe−O π bond.[35] Since the relative donor strength of the π_v^*_d_{xz} to d_{xz}_π_v^* CT transition in Table 3 is very similar for both the low-spin and the high-spin Fe−OO^{t}Bu complex (vide supra), the π_v^* covalency of both systems must be comparable. The calculated value for **1̃a** of 24% is in good agreement with the experimentally calibrated π_v^* covalency of about 20% for the low-spin compound.[17] In the B3LYP/LanL2DZ calculation of **1̃a**, a comparable value for the π_v^* covalency of 23% is obtained.

Further contributions to the Fe(III)−OO^{t}Bu bond are identified from the MO scheme in Figure 6. Since the π_v^b orbital does not interact with the d orbitals of iron (cf. Table 6; $\beta\langle 30\rangle$), these additional contributions are of σ type. Next in energy to the HOMO (π_v^*) of the ^{t}BuOO$^-$ ligand is the in-plane orbital π_h^*, which interacts with an hybridized d orbital of iron that is mainly of e_g type and therefore labeled d_σ. The corresponding bonding combination, π_h^*_d_σ, is mixed with the bonding combination of the out-of-plane π donor orbital of hydroxide and d_{yz}, labeled O(P)_d_{yz}. The two resulting MOs, $\beta\langle 42\rangle$ and $\beta\langle 41\rangle$,

(34) Regarding the nomenclature: "π_v^*_d_{xz}" denotes an MO that is a mixture of the orbitals π_v^* and d_{xz}; the one with the larger contribution to the MO comes first (in this example π_v^*). $\beta\langle 43\rangle$ refers to MO no. 43 with β spin.

Table 6. Charge Contributions of Important β Orbitals of **1̃a** Calculated with B88P86/Triple-ζ Basis

			Fe	O2		O3		C_{3t}	O8	ΣN
no.	label	energy (hartree)	d	s	p	s	p	s + p	s + p	s + p
$\beta\langle 50\rangle$	σ^*_d_σ	−0.1443	3	2	29	3	23	2	0	1
$\beta\langle 48\rangle$	d_σ + O2(p)	−0.2014	69	0	8	0	1	0	7	7
$\beta\langle 47\rangle$	d_σ_N(p)	−0.2181	73	0	3	0	0	0	2	15
$\beta\langle 46\rangle$	d_{xz}_π_v^*	−0.2587	69	0	18	0	6	0	3	0
$\beta\langle 45\rangle$	d_{yz}_O(p)	−0.2630	80	0	0	0	0	0	15	1
$\beta\langle 44\rangle$	d_{xy} (LUMO)	−0.2739	85	0	5	0	5	0	1	0
$\beta\langle 43\rangle$	π_v^*_d_{xz} (HOMO)	−0.3126	28	0	25	0	37	0	1	1
$\beta\langle 42\rangle$	O(p)_d_{yz}/π_h^*_d_σ	−0.3611	11	0	25	0	9	2	37	5
$\beta\langle 41\rangle$	O(p)_d_{yz}/π_h^*_d_σ	−0.3690	13	0	26	0	9	2	36	2
$\beta\langle 39\rangle$	π_v^b/π_v^*_d_{xz}	−0.3960	3	0	16	0	4	12	8	2
$\beta\langle 37\rangle$	N(p) + π_v^b	−0.4172	0	0	4	0	11	1	2	30
$\beta\langle 32\rangle$	π_h^b_d_σ	−0.4348	6	0	9	0	7	1	0	11
$\beta\langle 31\rangle$	π_h^b_d_σ	−0.4445	1	0	9	0	8	1	0	3
$\beta\langle 30\rangle$	π_v^b	−0.4591	1	0	13	0	15	0	0	3
$\beta\langle 26\rangle$	π_h^b_d_σ	−0.5174	2	0	11	2	18	13	7	3
$\beta\langle 24\rangle$	σb	−0.5395	0	2	16	0	18	16	1	3

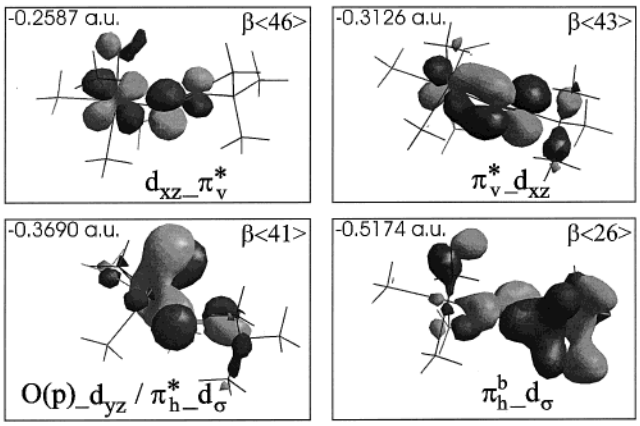

Figure 7. Contour plots of the molecular orbitals of **1̃a** (cf. Figure 6 and Table 6) corresponding to the most important interactions of the alkylperoxo donor (π_v^*, π_h^*, π_h^b) orbitals with the d functions of iron(III).

are equal mixtures of π_h^*_d_σ and O(P)_d_{yz} as given in Table 6 (Figure 7 shows the contour of $\beta\langle 41\rangle$). Both have about 12% iron d character. In addition, the π bonding orbital π_h^b interacts with a d orbital of iron. The bonding combination, π_h^b_d_σ ($\beta\langle 26\rangle$), is found at low energy and shows a small admixture of an e_g type function (cf. Table 6 and Figure 7). Finally, the O−O σ bonding orbital σ^b is essentially nonbonding to the metal. Summing up these contributions, the Fe−O σ bond in the high-spin complex **1̃a** is dominated by the O−O antibonding orbital π_h^*. The different σ interactions between the alkylperoxo ligand and iron(III) are summed up in the Fe−O antibonding e_g orbital d_σ_O2(p) ($\beta\langle 48\rangle$), which has about 9% contribution from the peroxide (cf. Table 6). Compared to the B88P86 calculation on low-spin $[Fe(TPA)(OH_2)(OO^tBu)]^{2+}$, the σ covalency is reduced by 70% in **1̃a**. The energy of the CT transition from π_h^*_d_σ ($\beta\langle 42\rangle$ and $\beta\langle 41\rangle$, cf . Figure 6 and Table 6) to d_σ_O2(p) ($\beta\langle 48\rangle$) in **1̃a** can be roughly estimated[36] at around 42 000 cm^{-1}, which is outside the spectroscopically accessible range in Figure 3.

In summary, the π_v^* orbital of the alkylperoxo ligand forms a strong π bond with the d_{xz} function of iron(III) which gives rise to an intense CT transition around 17 900 cm^{-1}. The covalency of this bond is reasonably described in the calculation compared to experiment. Other contributions to the Fe−O bond are σ donor interactions which predominantly involves the π_h^* interaction with d_σ. Compared to experiment, the calculated Fe−O force constant is too low, which indicates that σ bonding is underestimated in the calculation.

(B.3) Homolytic Cleavage of the O−O Bond. In this section, the reaction coordinate ΔO−O of the homolytic cleavage of the O−O bond is investigated for the model system $[Fe(NH_3)_4(OH)(OO^tBu)]^+$ in the three spin states $S = 5/2$ (**1̃a**), 3/2, and 1/2. Thia model system gives reasonable ground-state descriptions and reaction energies for the spin states $S = 1/2$ and 5/2 (cf. ref 17 and vide supra). The corresponding optimized structures for $S = 1/2$ and 5/2 have been used as a starting point for the potential energy surface (PES) scans. For $S = 3/2$, the geometry has been fully optimized with B3LYP/LanL2DZ, and the resulting structural parameters, charges, and spin densities are given in Table 4. Figure 8, top, shows the PES for O−O homolysis for the three spin states $S = 5/2$, 3/2, and 1/2 calculated with B3LYP/LanL2DZ. The $S = 1/2$ complex reacts to an Fe(IV)═O intermediate $[Fe(NH_3)_4(OH)(O)]^+$ with $S = 1$ and the ^{t}BuO• radical. The total energy of the products (at infinite distance) is given by the line at 30 kcal/mol.[17] Both the $S = 3/2$ and 5/2 systems react to the corresponding Fe(IV)═O intermediate with $S = 2$ in the calculation and the total energy of the products in this case is about 32 kcal/mol indicated by the top horizontal line.

The potential energy surface for the low-spin Fe(III)−alkylperoxo complex ($S = 1/2$) in Figure 8, top, shows a steep increase in energy on elongation of the O−O bond from the equilibrium distance (1.505 Å). At a r(O−O) of about 2 Å, the energy reaches a maximum and then gradually increases from about 2.8 Å on and asymptotically approaches the final energy at an infinite distance of the products. This gradual increase at long O−O distances is due to the gas-phase nature of the calculations: in vacuum, the two product molecules interact even at an O−O distance of 10 Å. In addition, polar solvents

(35) From B88P86 − ΔSCF calculations, the energy of this transition could not be obtained because the wave function always converged to lower lying excited states.

(36) The energy of this CT transition can be estimated from the averaged orbital energy difference Δe (about 36 000 cm^{-1}), adding an experimental scaling factor of 6000 cm^{-1}, which is estimated from the observed offset for the π charge transfer ($\Delta e = 11\,830$ cm^{-1} versus experimental CT energy of 17 900 cm^{-1}). This is due to the fact that Δe is not a good approximation to the CT transition energy for high-spin Fe(III), because of the large loss of exchange energy that occurs on transfer of an electron to the high-spin $[\alpha\text{-}d]^5$ manifold.

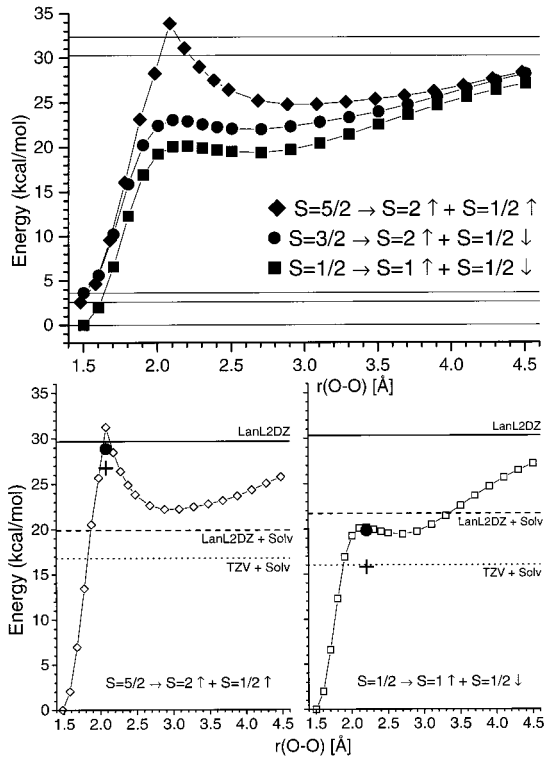

Figure 8. Reaction coordinate for the homolytic cleavage of the O−O bond calculated for model $[Fe(NH_3)_4(OH)(OO^tBu)]^+$ for $S = 1/2$, 3/2, and 5/2 with B3LYP/LanL2DZ. On the top, the PESs are given relative to the $S = 1/2$ complex set to 0 kcal/mol. The horizontal lines represent the energies of (from bottom to top): $S = 1/2$, $S = 5/2$, and $S = 3/2$ starting complexes, and products at infinite distance for Fe^{IV}═O with $S = 1$ and $S = 2$ (top). On the bottom, right, the $S = 1/2$ surface is shown with horizontal lines represent final reaction energies as indicated (calculated with B3LYP, see text). The symbols correspond to the relative energy at r(O−O) = 2.2 Å recalculated with LanL2DZ plus solvent (●) and TZV plus Solvent (+), respectively. On the bottom, left, the corresponding data are shown for the high-spin ($S = 5/2$) PES. The changes of the Fe−O bond length along the O−O reaction coordinate are given in Figure 1 of the Supporting Information.

lead to a large stabilization of the products relative to the Fe−OOR reactant,[17] which will influence the shape of the PES. This aspect is addressed in Figure 8, bottom right. Here, the PES for low-spin $[Fe(NH_3)_4(OH)(OO^tBu)]^+$ is shown again together with vertical lines indicating the dissociation limit for O−O homolysis calculated with (a) B3LYP/LanL2DZ (solid line), (b) B3LYP/LanL2DZ plus solvent effects (dashed line), and (c) B3LYP/TZV plus solvent effects (dotted line). As has been described previously, the inclusion of solvent effects leads to a large stabilization of the Fe^{IV}═O species and hence, the dissociation limit is strongly decreased for the two solvent calculations compared to the gas-phase result.[17] In addition, the energy at the potential transition state (r(O−O) = 2.2 Å) has been recalculated for LanL2DZ plus solvent (indicated with a dot (●) in Figure 8, bottom right) and TZV plus solvent (indicated with a cross). Importantly, the solvent stabilization at this point is comparable to the value obtained for the initial Fe−OOR complex such that the relative energy does not change much compared to the gas-phase PES. However, the energy difference to the dissociation limit is reduced by the solvent effect from 10.1 to 1.9 kcal/mol (LanL2DZ) and only 0.2 kcal/mol (TZV), respectively. This shows that the PES for the O−O homolysis of the low-spin complex ($S = 1/2$) first increases steeply and then levels off at an O−O distance of about 2.2 Å and reaches the final energy at the dissociation limit. Hence, there is no significant transition state on the PES. In summary, the homolytic cleavage of the O−O bond proceeds smoothly for the low-spin complex without a barrier on the PES.

The potential energy surface for the hypothetical Fe(III)−alkylperoxo complex with $S = 3/2$ calculated with B3LYP/LanL2DZ is shown in Figure 8, top. This surface closely resembles the one obtained for the low-spin complex. Hence, as in the low-spin case, there is no barrier on the PES for homolytic cleavage of the O−O bond for this spin state.

This is in contrast to the high-spin complex as shown in Figure 8, top. In this case, the energy steeply increases on elongation of the O−O bond from the equilibrium distance (1.482 Å) and reaches a maximum at r(O−O) = 2.1 Å. Here, the ascending PES of the Fe(III)−alkylperoxo complex crosses a surface that decreases in energy on further elongation of the O−O bond. Finally, at a r(O−O) of about 3.2 Å, the energy starts to increase again and asymptotically approaches the dissociation limit at large O−O distances. This final gradual increase in energy is related to the gas-phase nature of the calculations (vide supra). To evaluate a more realistic form of the energy surface, calculations have been applied that include solvent effects. Figure 8, bottom left, shows the PES from the B3LYP/LanL2DZ calculation, but here the energy is given relative to the high-spin $[Fe(NH_3)_4(OH)(OO^tBu)]^+$ reactant at 0 kcal/mol. The horizontal solid line on top corresponds to the gas-phase energy at the dissociation limit (infinite distance of the products). In this case, the actual barrier for the O−O homolysis is only 1.6 kcal/mol. Including solvation effects leads to a large stabilization of the Fe^{IV}═O product and, hence, decreased reaction energies for both the LanL2DZ (horizontal dashed line) and the TZV calculation (dotted line). On the other hand, the solvent stabilization at the maximum of the PES (r(O−O) = 2.1 Å) is comparable to the initial Fe(III)−OO^tBu complex, such that the resulting relative energies at this point for LanL2DZ plus solvent (indicated with a dot (●) in Figure 8, bottom left) and TZV plus solvent (indicated with a cross) are close to the gas-phase PES. Therefore, the reaction barrier increases to 9.0 kcal/mol (LanL2DZ) and even 10 kcal/mol (TZV) when solvation effects are included.

The finding that the reaction coordinate for the homolytic cleavage of the O−O bond has a barrier for the high-spin but not for the low-spin complex marks an important difference in the reactivity of these systems. We now consider the electronic origin of this barrier. Figure 1 of the Supporting Information shows how the Fe−O bond length changes along the reaction coordinate ΔO−O. Importantly, whereas there is a smooth and gradual shortening of the Fe−O bond for $S = 1/2$ and 3/2, the high-spin complex shows a very different behavior. Here, the Fe−O distance remains above 1.9 Å and then at r(O−O) = 2.1 Å rapidly decreases to 1.68 Å. This can be interpreted in the sense that, on elongation of the O−O bond, the system remains in an electronic structure that resembles the initial Fe(III)−OO^tBu state until this PES crosses the descending surface that has an Fe^{IV}═O like electronic structure. At this point, the system enters the product-like PES associated with a large change of the Fe−O bond length. Importantly, this means that for the high-spin complex the two educt- and product-like energy surfaces do not interact.

Analysis of the MO diagram of the high-spin complex around the maximum of the barrier provides insight into the electronic structural origin of this finding. Scheme 1 shows simplified sketches of the MO schemes at r(O−O) = 1.98 Å (left) and r(O−O) = 2.08 Å (right). Note that, at O−O distances r(O−O) > 1.8 Å, the two π bonds between the two alkylper-

Scheme 1

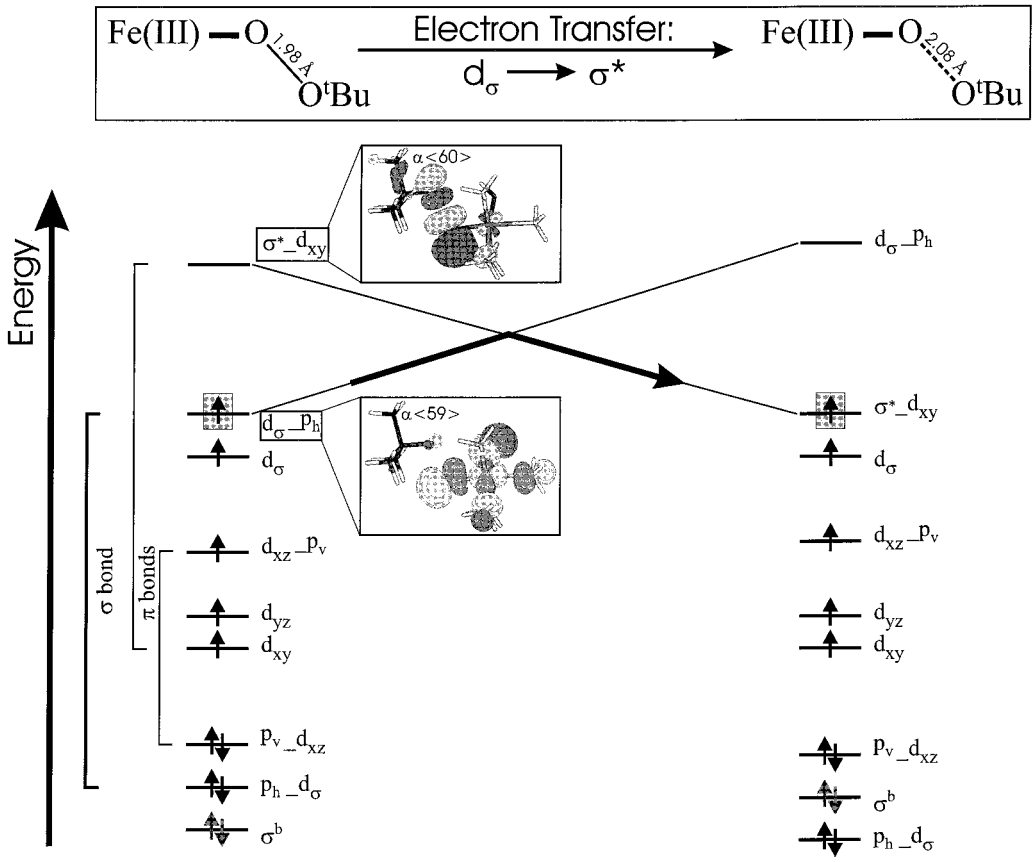

oxide oxygens collapse, which leads to the formation of two localized donor orbitals on the coordinating oxygen atom: p_v (originating from π_v^*/π_v^b) being a π donor and p_h (originating from π_h^*/π_h^b) which is a σ donor. To homolytically cleave the O−O bond, one electron has to be transferred from a d function of iron(III) to the σ^* orbital of alkylperoxide. In the high-spin case leading to the Fe^{IV}═O product with $S = 2$, the electron comes from the e_g orbital that interacts with p_h, d_σ_p_h in Scheme 1. The σ^* orbital itself forms a π bond with d_{xy} as shown in Scheme 1 (σ^*_d_{xy}). On elongation of the O−O bond, σ^* is lowered in energy and crosses d_σ and at this point the electron is transferred. *Importantly, the two redox active orbitals in this process,* d_σ *(donor) and* σ^**(acceptor),* **do not** *interact.* Therefore, this process corresponds to an allowed orbital crossing as indicated in Scheme 1 (the transferred electron is highlighted). Hence, the resulting barrier on the PES can be classified as an orbital barrier. The removal of the electron from the antibonding orbital d_σ_p_h leads to a distinct strengthening of the Fe−O bond, which is the reason for the dramatic decrease of the Fe−O distance after the PES crossing (cf. Figure 1 of the Supporting Information).

In contrast to the high-spin system, there is a gradual change of the electronic structure in going from the initial Fe(III)−OO^{t}Bu system to the final Fe^{IV}═O product for both the low-spin and the $S = 3/2$ complexes (cf. Figure 8 and Figure 1 of the Supporting Information). This is reflected by the gradual change of the Fe−O bond length and the absence of a barrier on the PES for these spin states. Scheme 2 shows sketches of the electronic structures of low-spin Fe(III)−OO^{t}Bu at r(O−O) ∼ 1.9 Å (left), correlated to the MO diagram of the Fe^{IV}═O product with $S = 1$ (right, see ref 17). The notation of the orbitals is the same as in Scheme 1. For the Fe^{IV}═O product, the O−O σ bond has been eliminated, leaving a third lone pair donor orbital on the oxo group, labeled p_σ (originating from σ^b/σ^*), which forms a π bond with d_{xy}. p_σ' is the corresponding p function on the ^{t}BuO• radical which is singly occupied. The plots in the middle of Scheme 2 show contours of important orbitals at r(O−O) = 2.2 Å which corresponds to the local maximum on the PES in Figure 8, top. In the case of the low-spin complex, one electron is transferred from d_{xy} to σ^* in the homolytic cleavage of the O−O bond leading to the Fe^{IV}═O product with $S = 1$. *Importantly, in this case the two redox active orbitals,* d_{xy} *(donor) and* σ^**(acceptor),* **do** *interact* as can be seen from Scheme 2. In the electronic structure of the Fe(III)−OO^{t}Bu complex with the elongated O−O bond (Scheme 2, left), there is a distinct π interaction between σ^* and d_{xy}. At r(O−O) = 2.2 Å, these orbitals are about equally mixed as illustrated in the contour plots in Scheme 2 with d_{xy}_σ^* being the bonding and σ^*_d_{xy} being the antibonding combination. Therefore, the O−O bond homolysis for the low-spin complex corresponds to a process with a forbidden orbital crossing. The "repulsive" interaction of σ^* and d_{xy} leads to a lowering of the barrier as illustrated with an arrow in Scheme 2. Another factor that contributes to the stabilization of the low-spin system along the O−O homolysis reaction coordinate is the gradual formation of the strong Fe−O σ bond between d_σ and p_h (illustrated by the contour plot of the corresponding antibonding combination, d_σ_p_h (at r(O−O) = 2.2 Å), in Scheme 2).

(B.4) Homolytic Cleavage of the Fe−O Bond. An alternative decay pathway for the Fe(III)−alkylperoxo complexes is the homolytic cleavage of the Fe−O bond leading to a five-coordinate Fe(II) complex and an alkylperoxyl radical:

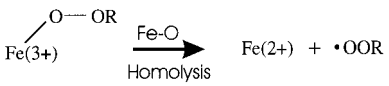

Scheme 2

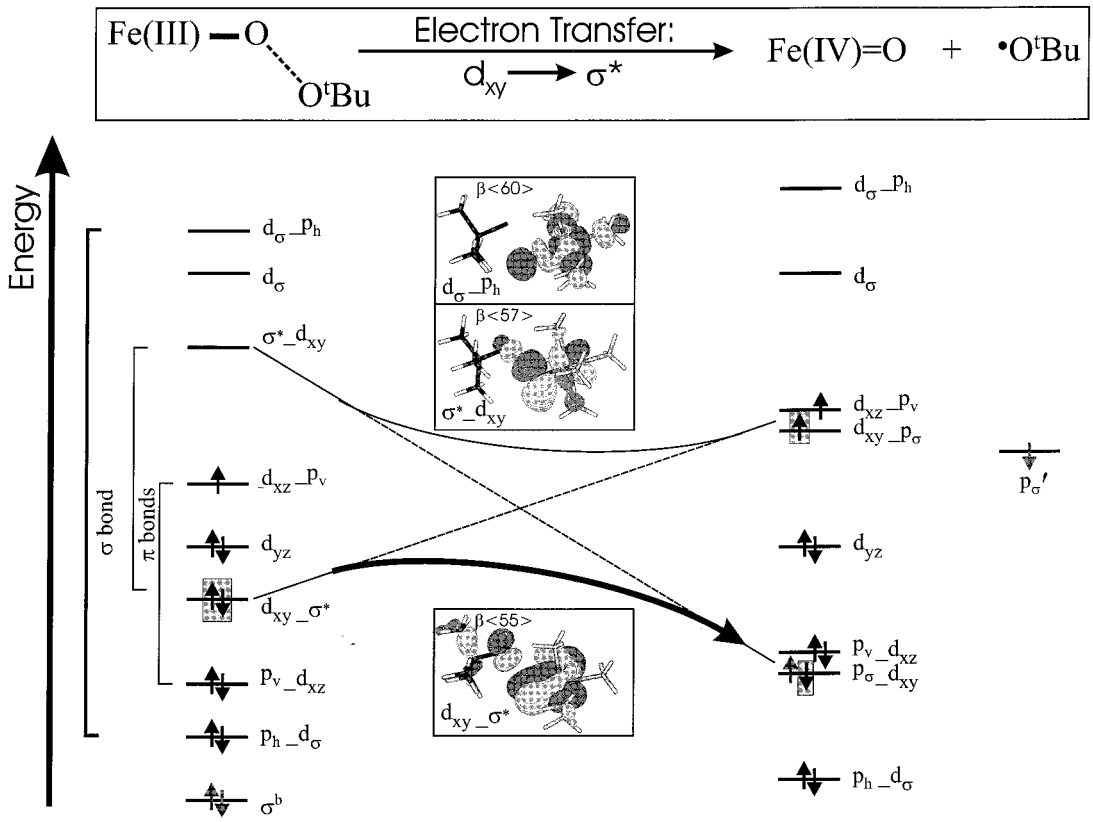

Table 7. Thermodynamics of the Homolytic Cleavage of the Fe−O Bond in **1̃a** (Calculated with B3LYP)[a]

reactant	product[b]	Δ*E* (kcal/ mol) LanL2	Δ*E* (kcal/ mol) + Solv	Δ*E* (kcal/ mol) TZV	Δ*E* (kcal/ mol) + Solv	−*T*Δ*S* (kcal/mol)	ZPCE (kcal/mol)
1̃a (*S* = 1/2)	*S* = 0	57.1	52.1	59.6	54.4	−16.2	−3.3
	S = 1	44.4	39.8	45.1	40.3	−15.7	−3.7
1̃a (*S* = 5/2)	*S* = 2	27.0	22.2	31.9	27.4	−14.2	−2.2

[a] Solv: including a solvent sphere in the calculation using the polarized continuum model (PCM) and acetonitrile as solvent; entropy (T = 298 K) and zero point correction energy (ZPCE) calculated using the LanL2DZ basis set. [b] Spin state of the $[Fe(NH_3)_4(OH)]^+$ complex; the •OOR radical has $S' = 1/2$. Total Spin: $S_{tot.} = S \pm S'$.

There is some evidence from the DFT calculations that this mechanism could be relevant for the high-spin systems: in the case of high-spin $[Fe(NH_3)_4(OH_2)(OO^tBu)]^{2+}$ (**1̃**), the optimized structure corresponds to an Fe(II)−alkylperoxyl ground state (vide supra). To calculate the thermodynamic data and the reaction coordinate for the Fe−O homolysis, B3LYP calculations have been performed on the model system $[Fe(NH_3)_4(OH)(OO^tBu)]^+$ in the high-spin (**1̃a**) and low-spin state for the following reaction:

$$[Fe(NH_3)_4(OH)(OO^tBu)]^+ \rightarrow [Fe(NH_3)_4(OH)]^+ + \bullet OO^tBu$$

For the two reactants, the optimized structures from B3LYP/LanL2DZ calculations have been used (vide supra and ref 17), and the structure of the product complex $[Fe(NH_3)_4(OH)]^+$ has been fully optimized for the three spin states S = 0, 1, 2 on this level of theory. Table 7 shows the calculated energies for the Fe−O homolysis considering only spin-allowed reactions. For the high-spin Fe(III)−OO^{t}Bu complex, yielding the S = 2 product, the B3LYP/LanL2DZ calculations including solvent effects predict a reaction energy of +22 kcal/mol.[37] Using the TZV basis set on the LanL2DZ structures does not lead to lower reaction energies as shown in Table 7. Taking into account the large entropy gain on splitting of the Fe−O bond of about 14 kcal/mol and zero point corrections, the total free energy of this reaction is about +5 kcal/mol. In the case of the low-spin system, the Fe−O homolysis is much more endothermic. The reaction energy is calculated to be +40 kcal/mol for the S = 1 and +52 kcal/mol for the S = 0 product, respectively, using LanL2DZ and including solvent effects. Importantly, the additional +17 kcal/mol (S = 1 product) and +30 kcal/mol (S = 0 product) compared to the high-spin complex (S = 2 product) mainly reflect the energy differences of the three different spin states of the five-coordinate $[Fe(NH_3)_4(OH)]^+$ product complex. Including entropy and zero point corrections, the Fe−O homolysis is still endothermic by at least 20 kcal/mol (for the S = 1 product) in terms of free energy for the low-spin complex.[38]

Figure 2 of the Supporting Information shows the PES along the ΔFe−O reaction coordinate calculated with B3LYP/

(37) Compared to the O−O homolysis the solvent stabilization is smaller, because the five-coordinate product complex is not as strongly polarized as the Fe(IV)=O species.

(38) Note that under the experimental reaction conditions, it can be expected that the five-coordinate product is actually protonated. Assuming that the pK_A of this species is around 7−9, this would add about −10 kcal/mol to the reaction energy. This leads to a negative free energy in the high-spin case and, hence, a driving force for Fe−O homolysis. However, this reaction would still be very unfavorable for the low-spin complex.

LanL2DZ for high-spin and low-spin $[Fe(NH_3)_4(OH)(OO^tBu)]^+$. Here, the energy is given in kilocalories per mole relative to the low-spin complex. Note that the gradual increase of both energy surfaces at large r(Fe−O) derives from the gas-phase nature of the calculations (vide supra). As can be seen from Figure 2 of the Supporting Information, no barrier occurs on the PES for the Fe−O homolysis for both the high-spin and low-spin Fe(III)−OO^tBu complexes. This is due to the fact that, in both cases, the electron is transferred from the alkylperoxo ligand to Fe(III) through their strong π bond mediated by π_v^* and d_{xz} (vide supra). Therefore, the redox active orbitals, π_v^* (donor) and d_{xz} (acceptor), strongly interact with each other, giving rise to a forbidden orbital crossing along the reaction coordinate and, hence, a low-barrier process.

In summary, the homolytic cleavage of the Fe−O bond is a thermodynamically competent reaction for the high-spin complex having a free reaction energy of about +5 kcal/mol and no barrier on the PES. In contrast, the Fe−O homolysis for the low-spin system has a free energy of about +20 kcal/mol and, hence, is thermodynamically unfavorable. This is due to the low-spin nature of the five-coordinate ferrous product. These results indicate another important potential difference in the reactivity of the low-spin and the high-spin Fe(III)−OO^tBu complexes.

Discussion

The resonance Raman spectrum of high-spin $[Fe(6\text{-}Me_3TPA)(OH_x)(OO^tBu)]^{x+}$ (**1**) shows four peaks at 876, 842, 637, and 469 cm^{-1} that have been assigned using isotope perturbations. The two features at 876 and 842 cm^{-1} correspond to the O−O and the symmetric C−C stretch of the *tert*-butyl group that are about equally mixed. Their intensity, however, derives solely from the resonance enhancement of the O−O stretch. The peak at 637 cm^{-1} is identified with the Fe−O stretch and the feature at 469 cm^{-1} is assignedto a combined O−C−C and C−C−C bend of the *tert*-butyl group that gains its resonance intensity from a large admixture of the Fe−O stretch. These vibrational features are very similar to the spectra of [(L3)Cu(OO^tBu)] that have been assigned accordingly based on the analysis presented here.[39] These results are also in agreement with the assignment of the Raman spectra of low-spin $[Fe(TPA)(OH_x)(OO^tBu)]^{x+}$.[17] The force constants of the Fe(III)−OO^tBu subunit have been determined from normal coordinate analysis. Importantly, complex **1** has a strong O−O (force constant k = 3.55 mdyn/Å) and weak Fe−O bond (k = 2.87 mdyn/Å).

The UV−vis spectrum of **1** shows a medium intense absorption band around 560 nm that corresponds to a positive feature in the MCD. All four vibrations at 876, 842, 637, and 469 cm^{-1} are resonance enhanced with respect to this absorption which can therefore be assigned as an alkylperoxo to Fe(III) charge-transfer transition. From the DFT calculations, this feature corresponds to a π bond between the π_v^* orbital of the alkylperoxide and the d_{xz} orbital of iron. The 560 nm CT transition of **1** has a relative donor strength of 0.5. In comparison, the Cu(II)−alkylperoxo complex [(L3)Cu(OOCm)] has a corresponding absorption with a relative donor strength of 1.1, which indicates that the metal−O π bond is stronger in the latter case. On the other hand, both complexes have about the same metal−O force constant. This indicates that there must be additional contributions to the Fe−O bond in **1**. Spectroscopically, no corresponding CT transition could be identified in the accessible energy region. Hence, DFT calculations have been used to identify the additional bonding interactions between Fe(III) and alkylperoxide. These arise from ligand σ donor orbitals that interact with an e_g function of iron, where the in-plane π_h^* orbital gives rise to the dominant contribution to the Fe−O σ bond.

The electronic structure of the high-spin complex **1** described above shows important differences compared to the analogous low-spin system $[Fe(TPA)(OH_x)(OO^tBu)]^{x+}$. The force constants obtained from NCA show that the low-spin complex has a stronger Fe−O (k = 3.53 mdyn/Å) than O−O bond (k = 2.92 mdyn/Å),[17] which is *inverse* to the order of bond strengths that have been found for **1**. This indicates an important difference in the electronic structure of these systems. Both complexes show a characteristic absorption band in the visible region, which corresponds to the π bond between alkylperoxide and Fe(III). This feature is located around 560 nm for the high-spin and around 600 nm for the low-spin system. Importantly, both absorption bands have the same relative donor strength of about 0.5 (cf. ref 17). Therefore, *the π bond between Fe(III) and the alkylperoxo ligand has the same covalency in these two systems*. Since the Fe−O bond is shorter by ∼0.1 Å in the low-spin complex, the overlap and, hence, the bonding interaction between π_v^* and d_{xz} is somewhat larger in this case. To obtain the same covalency, the fragment orbitals π_v^* and d_{xz} must be closer in energy in the high-spin complex, which is in agreement with the observed trend from the DFT calculations. The fact that the CT energy is larger for the high-spin complex reflects the large exchange stabilization of the high-spin d^5 shell which is partially lost in the CT transition. Since the Fe(III)−OO^tBu π bond has a comparable strength in the high-spin and the low-spin complex, there must be additional contributions to the Fe−O bond that are stronger for the low-spin system in order to obtain the larger Fe−O force constant. This additional Fe−O bond is of the σ type. The dominant contribution to this Fe−O σ bond is shifted from O−O bonding orbitals in the low-spin case[17] to π_h^* in the high-spin system, which explains why the O−O bond is stronger in **1**. Importantly, the total σ donor interaction is clearly weaker in **1** which is due to the high-spin d^5 electron configuration where both e_g orbitals are singly occupied and have repulsive interactions with the σ electron density on the ligands. Therefore, the lower Fe−O force constant in **1** is due to the loss in σ bonding.

The differences in the electronic structure of low-spin and high-spin Fe(III)−OO^tBu complexes are reflected in their different reactivities. Experimentally, the low-spin complex $[Fe(TPA)(OH_x)(OO^tBu)]^{x+}$ has been shown to undergo homolytic cleavage of the O−O bond,[22,23] which corresponds to a thermoneutral reaction in terms of free energy for this system.[17] In this study, the potential energy surface of O−O homolysis is investigated for the high-spin and low-spin complexes and related to their electronic structures. In the low-spin case, there is a smooth and gradual transformation of the Fe(III)−alkylperoxo complex to the Fe^{IV}═O product (S = 1) indicated by the gradual change of the Fe−O bond length and the absence of a barrier on the PES. Along the reaction coordinate, one electron is transferred from the d_{xy} orbital of iron to σ^*. Importantly, these orbitals strongly interact with each other forming a π bond (cf. Scheme 2). This leads to an interaction of the initial, educt-like and the final, product-like electronic states along the reaction coordinate (cf. Figure 8). Therefore, this process corresponds to a forbidden orbital crossing of d_{xy} and σ^*, and no barrier is observed. A further stabilization arises from the fact that the strong Fe−O σ bond in the Fe^{IV}═O product is gradually formed from the first step of the O−O

(39) Chen, P.; Fujisawa, K.; Solomon, E. I. *J. Am. Chem. Soc.* **2000**, *122*, 10177.

homolysis reaction. This is in contrast to the high-spin complex which has a kinetic barrier of about 10 kcal/mol for O−O bond homolysis. The barrier on the PES is correlated with an abrupt change of the Fe−O bond length along the reaction coordinate (cf. Figure 1 of the Supporting Information). This is due to the fact that the two redox active orbitals, d_σ (donor) and σ^* (acceptor), do not interact with each other (cf. Scheme 1), which corresponds to an allowed orbital crossing. Hence, the system abruptly transfers from the initial to the final electronic state at the crossing point of the corresponding energy surfaces (cf. Figure 8). In addition, since both e_g orbitals are initially occupied, the strong Fe−O σ bond cannot form on the educt-like PES which is energetically unfavorable. This is another limitation for the O−O homolysis in the high-spin complex. Note that the electronic structure of the low-spin complex having a strong Fe−O and weak O−O bond, which is in contrast to the high-spin system, reflects the transition state for O−O bond homolysis. The nascent transition-state character in the low-spin ground state can be identified with the developing Fe−O σ bond, which is already partially formed in the starting complex.[17]

This marks an important difference in the reactivity of the two Fe(III)−OO^{t}Bu complexes: whereas the low-spin complex is kinetically competent for O−O bond homolysis, there is a barrier for this reaction on the high-spin surface. Therefore, one would expect the high-spin complex to undergo a different reactivity. In general, different reactivities for different spin states of the same complex have been considered, for example in gas-phase experiments,[40] organometallic systems[41] and P450 chemistry.[42] The results of Armentrout and co-workers indicate that the spin state is conserved along a reaction coordinate.[40a,b] On the other hand, surface hopping between states of different total spin has been proposed for gas-phase and P450 chemistry.[40c,42c] In the model presented here, a possible mechanism for the high-spin complex to overcome the barrier on the PES would be a crossover to the $S = 3/2$ surface. Since both systems react to the Fe^{IV}═O product in the same spin state ($S = 2$), there must be a crossing point of the energy surfaces before the maximum on the $S = 5/2$ PES, i.e., at $r(O-O) < 2.1$ Å. The $^6A_1$ ground state of the high-spin system strongly interacts with a component of the $^4T_1$ excited state (which is the ground state of the $S = 3/2$ system) by spin−orbit coupling (SOC). This could enable the $S = 5/2$ system to cross to the $S = 3/2$ surface and avoid the barrier on the PES. However, there is an important difference between the $S = 5/2$ and the $S = 3/2$ surfaces at the crossing point that has to be taken into account. As described above, there is no interaction between the educt-like and product-like energy surfaces in the $S = 5/2$ case because of the allowed orbital crossing. This means that, on elongation of the O−O bond, the energy strongly increases because of the weakened interaction between the oxygen atoms and the iron(III) center does not help stabilize this. The Fe−O bond cannot contract (cf. Figure 1 of the Supporting Information and vide infra), and the system stays in a high-spin ferric-like electronic state. This is in contrast to the $S = 3/2$ state where the surfaces interact. This means that, along the reaction coordinate, the electronic structure of the $S = 3/2$ system corresponds to a mixture of the initial, ferric $S = 3/2$ state ($\psi_1 = |d_{xy}^\alpha d_{xz}^\alpha d_{yz}^\alpha d_\sigma^\alpha d_{xy}^\beta|$) and the final, iron(IV) $S = 2$ state, where one electron has been transferred to an oxygen p_σ orbital ($\psi_2 = |d_{xy}^\alpha d_{xz}^\alpha d_{yz}^\alpha d_\sigma^\alpha p_\sigma^\beta|$):

$$\Psi^{S=3/2} = c_1|d_{xy}^\alpha d_{xz}^\alpha d_{yz}^\alpha d_\sigma^\alpha d_{xy}^\beta| + c_2|d_{xy}^\alpha d_{xz}^\alpha d_{yz}^\alpha d_\sigma^\alpha p_\sigma^\beta|$$

Importantly, whereas SOC between the ferric $S = 5/2$ state and ψ_1 is large, as described above, the corresponding SOC matrix element between the ferric $S = 5/2$ state and ψ_2 represents a two-center SOC integral and, hence, is of negligible size.[43] Related to this, there is also a large geometry difference in the Fe−O bond length at the crossing point when going from the $S = 5/2$ to the $S = 3/2$ state, which will further introduce an energy barrier. Both effects will eliminate surface hopping of the high-spin state along the reaction coordinate.

The general scheme derived here can be used to predict barriers on the PES for homolytic cleavage of the O−O bond in related systems. In the case of Cu(II)−alkylperoxo complexes, O−O homolysis has been discussed as a possible reaction pathway.[39] In the initial complex, the half-occupied orbital $d_{x^2-y^2}$ interacts with π_v^* forming a π bond,[39] and this interaction is maintained in the Cu^{III}═O product where the empty $d_{x^2-y^2}$ function forms a π bond with the corresponding lone pair on the oxo group.[17,44] The conservation of this interaction along the reaction coordinate is energetically favorable and should lead to some stabilization of the intermediate species. However, the redox active orbitals for O−O homolysis are $d_{x^2-y^2}$ (donor) and σ^* (acceptor), which do not interact. Hence, this process corresponds to an allowed orbital crossing and goes along with a barrier on the PES, which makes this reaction unlikely. Another interesting comparison can be made with high-spin Fe(II)−alkylperoxo and −hydroperoxo complexes. The latter Fe(II)−OOH systems are involved in Fenton type chemistry[45] and result from coordination of H_2O_2 to an iron(II) center. In this case, the reaction product of the O−O homolysis is a high-spin Fe(III)−oxo complex, which, after protonation, yields the final Fe(III)−OH product. Along the reaction coordinate of O−O homolysis, one electron is transferred from a t_{2g} orbital of iron to σ^*. As in the low-spin Fe(III)−OO^{t}Bu case, these orbitals strongly interact, which indicates that there should be no significant barrier on the PES for this process.

Since the homolytic cleavage of the O−O bond has a barrier on the PES for **1**, this reaction is unlikely to occur. Hence, there must be a different decay pathway for high-spin Fe(III)−OO^{t}Bu complexes. One reasonable alternative is the homolytic cleavage of the Fe−O bond, as has been proposed for **1**.[46] From

(40) (a) Elkind, J. L.; Armentrout, P. B. *J. Am. Chem. Soc.* **1986**, *108*, 2765. (b) Armentrout, P. B. *Science* **1991**, *251*, 175. (c) Schröder, D.; Shaik, S.; Schwarz, H. *Acc. Chem. Res.* **2000**, *33*, 139.

(41) (a) Poli, R. *Chem. Rev.* **1996**, *96*, 2135. (b) Keogh, D. W.; Poli, R. *J. Am. Chem. Soc.* **1997**, *119*, 2516.

(42) (a) Toy, P. H.; Newcomb, M.; Hollenberg, P. F. *J. Am. Chem. Soc.* **1998**, *120*, 7719. (b) Shaik, S.; Filatov, M.; Schröder, D.; Schwarz, H. *Chem. Eur. J.* **1998**, *4*, 193. (c) de Visser, S. P.; Ogliaro, F.; Harris, N.; Shaik, S. *J. Am. Chem. Soc.*, in press.

(43) Taking into account that the crossing point between the $S = 5/2$ and the $S = 3/2$ energy surface is further along the reaction pathway but before the maximum on the high-spin PES, the $S = 3/2$ state predominantly corresponds to ψ_2 (>60%), which strongly reduces SOC.

(44) Chen, P.; Solomon, E. I. Unpublished data. The combination of the trigonally distorted tetrahedral ligand field around copper together with one strongly π bonding ligand leads to an electronic structure where the $d_{x^2-y^2}$ orbital (quantization along the trigonal axis) is highest in energy. The strong π donor is then oriented along the axis that bisects x and y.

(45) (a) Walling, C. *Acc. Chem. Res.* **1975**, *8*, 125. (b) Sheu, C.; Richert, S. A.; Cofre, P.; Ross, J., B.; Sobkowiak, A.; Sawyer, D. T.; Kanofsky, J. R. *J. Am. Chem. Soc.* **1990**, *112*, 1936.

(46) Kim, J.; Zang, Y.; Costas, M.; Harrison, R. G.; Wilkinson, E. C.; Que, L., Jr. *J. Biol. Inorg. Chem.* **2001**, *6*, 275.

(47) Pate, J. E.; Cruse, R. W.; Karlin, K. D.; Solomon, E. I. *J. Am. Chem. Soc.* **1987**, *109*, 2624.

(48) Baldwin, M. J.; Ross, P. K.; Pate, J. E.; Tyeklar, Z.; Karlin, K. D.; Solomon, E. I. *J. Am. Chem. Soc.* **1991**, *113*, 8671.

(49) Brunold, T. C.; Tamura, N.; Kitajima, N.; Moro-oka, Y.; Solomon, E. I. *J. Am. Chem. Soc.* **1998**, *120*, 5674.

(50) Neese, F.; Solomon, E. I. *J. Am. Chem. Soc.* **1998**, *120*, 12829.

(51) Ory, H. A. *Anal. Chem.* **1960**, *32*, 509.

the DFT calculations, this reaction is endothermic by about 20 kcal/mol if solvent effects are included. Taking the entropy gain upon splitting of the Fe−O bond and zero point vibrational corrections into account, the Fe−O homolysis is endothermic by about 5 kcal/mol in terms of free energy. A possible protonation of the five-coordinate product would further contribute to the thermodynamic driving force of this reaction. In contrast, the Fe−O homolysis is endothermic by at least an additional 15 kcal/mol for the low-spin complex and, hence, energetically unfavorable. Considering the reaction coordinate, there is no barrier on the PES for the homolytic cleavage of the Fe−O bond for both the high-spin and the low-spin complex. Therefore, the Fe−O homolysis is a reasonable reaction for the high-spin Fe(III)−OO^{t}Bu complex and could be the decay pathway of this species. Note that a similar decay pathway (Cu−O homolysis) has been proposed for Cu(II)−alkylperoxo complexes.[39]

In summary, these spectroscopic and theoretical results reveal an important difference between the high-spin and low-spin Fe(III)−OO^{t}Bu complexes: whereas the low-spin system has a strong Fe−O and a weak O−O bond, this order is reversed for the high-spin complex. These electronic structures reflect the different reactivities of these systems. Whereas the low-spin complex is energetically and kinetically competent to undergo homolytic cleavage of the O−O bond, there is a barrier for this reaction on the high-spin surface, which reflects an allowed state crossing. Alternatively, Fe−O homolysis is an energetically reasonable reaction for the high-spin complex, whereas it is thermodynamically unfavorable for the low-spin system due to the instability of the low-spin five-coordinate product complex.

Acknowledgment. This work was supported by the National Instituts of Health (Grants GM-40392 to E.I.S. and GM-33162 to L.Q.). N.L. thanks the Deutscher Akademischer Austauschdienst (DAAD) for a postdoctoral fellowship.

Supporting Information Available: Text describing the experimental and computational procedures, figures showing a schematic MO diagram of the ^{t}BuOO$^-$ ligand, the change of the Fe−O bond length along the ΔO−O reaction coordinate, the PES for Fe−O homolysis and corresponding O−O bond length changes, and the fully optimized structures of high-spin $[Fe(NH_3)_4(OH_2)(OO^tBu)]^{2+}$ (**1̃**) and high-spin $[Fe(Ime)_3(NH_3)(OH_2)(OO^tBu)]^{2+}$, and tables of the calculated and experimental (QCA-NCA) force constants, the excited-state distortions from Heller theory, calculated geometric parameters, charges, and spin densities of several model systems, Cartesian coordinates of the optimized structures of $[Fe(NH_3)_4(OH)(OO^tBu)]^+$ in the high-spin (**1̃a**) and the $S = 3/2$ state, complete force field of **1̂a** used for NCA, and Cartesian coordinates of the optimized structures of $[Fe(NH_3)_4(OH)]^+$ for $S = 0-2$ (PDF). This material is available free of charge via the Internet at http://pubs.acs.org.

JA011450+

(52) Butwill Bell, M. E.; Laane, J. *Spectrochim. Acta* **1972**, *28A*, 2239.